To appear in The Astrophysical Journal: submitted Oct 2, '98; accepted Dec 15, '98
Preprint typeset using LaTeX style emulateapj v. 04/03/99

PROPERTIES OF THE INTRACLUSTER MEDIUM IN AN ENSEMBLE OF NEARBY GALAXY CLUSTERS

Joseph J. Mohr[1,2,3,4] Benjamin Mathiesen[2] & August E. Evrard[2]
[1]Department of Astronomy and Astrophysics, University of Chicago, Chicago, IL 60637
[2]Department of Physics & [3]Department of Astronomy, University of Michigan, Ann Arbor, MI 48109
To appear in The Astrophysical Journal: submitted Oct 2, '98; accepted Dec 15, '98

ABSTRACT

We present a systematic analysis of the intracluster medium (ICM) in an X-ray flux limited sample of 45 galaxy clusters. Using archival ROSAT PSPC data and published ICM temperatures, we present best fit double and single β model profiles, and extract ICM central densities and radial distributions. We use the data and an ensemble of numerical cluster simulations to quantify sources of uncertainty for all reported parameters.

We examine the ensemble properties within the context of models of structure formation and feedback from galactic winds. We present best fit ICM mass-temperature M_{ICM}-$\langle T_X \rangle$ relations for M_{ICM} calculated within r_{500} and $1h_{50}^{-1}$ Mpc. These relations exhibit small scatter (17%), providing evidence of regularity in large, X-ray flux limited cluster ensembles. Interestingly, the slope of the M_{ICM}-$\langle T_X \rangle$ relation (at limiting radius r_{500}) is steeper than the self-similar expectation by 4.3σ. We show that there is a mild dependence of ICM mass fraction f_{ICM} on $\langle T_X \rangle$; the clusters with ICM temperatures below 5 keV have a mean ICM mass fraction $\langle f_{ICM} \rangle = 0.160 \pm 0.008$ which is significantly lower than that of the hotter clusters $\langle f_{ICM} \rangle = 0.212 \pm 0.006$ (90% confidence intervals). In apparent contradiction with previously published analyses, our large, X-ray flux limited cluster sample provides no evidence for a more extended radial ICM distribution in low $\langle T_X \rangle$ clusters down to the sample limit of 2.4 keV.

By analysing simulated clusters we find that density variations enhance the cluster X-ray emission and cause M_{ICM} and f_{ICM} to be overestimated by $\sim$12%. Additionally, we use the simulations to estimate an f_{ICM} depletion factor at r_{500}. We use the bias corrected mean f_{ICM} within the hotter cluster subsample as a lower limit on the cluster baryon fraction. In combination with nucleosynthesis constraints this measure provides a firm upper limit on the cosmological density parameter for clustered matter $\Omega_M \leq (0.36 \pm 0.01) h_{50}^{-1/2}$.

Subject headings: galaxies: clusters: general — intergalactic medium — cosmology

1. INTRODUCTION

The properties of galaxy cluster virial regions provide powerful constraints on models of structure formation and evolution. For example, evidence for continuing accretion in nearby clusters constrains the cosmological density parameter Ω_0 and the slope of the power spectrum of density perturbations $P(k)$ on cluster scales. Combining the baryon fraction within cluster virial regions with nucleosynthesis constraints on the baryon to photon ratio provides an estimate of the cosmological density parameter for clustered matter Ω_M. An emerging theoretical consensus that dissipationless collapse produces haloes which conform to a "universal" density profile (Navarro, Frenk, & White 1997) implies that measurements of cluster virial structure provide constraints on the nature of dark matter. Therefore, systematic, high precision analyses of large, well defined cluster samples can potentially enjoy broad and lasting impact.

There are several tools available to probe galaxy cluster virial regions. One can use gravitational lensing to study the characteristics of the clustered mass directly. At the present time, typical cluster weak lensing maps have peak signal to noise of $\sim$10 even at disappointingly low angular resolutions (e.g. Fischer & Mohr in prep), making it difficult to resolve differences between observed profiles and the NFW prediction. Studies of strong lensing can provide extremely detailed constraints on the structure of cluster cores (Tyson, Kochanski & Dell'Antonio 1998), but the required alignments of lens, source and observer occur in few clusters. Dynamical studies using galaxies can potentially resolve the dark matter structure and galactic orbits simultaneously, but doing so requires such a large galaxy sample that data from multiple clusters must be rescaled and stacked (e.g. Carlberg et al 1997), precluding tests of anything except average properties of cluster mass profiles. Archival ROSAT PSPC X-ray images of nearby galaxy clusters are of sufficient quality that high precision studies of the ICM in individual clusters are possible. Moreover, it is straightforward to study a large, well defined cluster ensemble, making it possible to compare the structure of high and low mass clusters and to *quantify* departures from self similarity.

Here we present a precision analysis of the intracluster medium in 45 nearby clusters. Our goals include (i) a study of cluster regularity, (ii) a quantitative characterization of the ICM mass-temperature (M_{ICM}-$\langle T_X \rangle$) relation for comparison to future structure formation and galaxy formation simulations, (iii) a definitive test of whether the ICM mass fraction f_{ICM} and radial distribution vary with cluster mass, and (iv) an improved measure of $\langle f_{ICM} \rangle$,

[4]AXAF Fellow

leading to an upper limit on the cosmological density parameter Ω_M.

Our technique is a synthesis of profile fitting methods applied to elliptical galaxies (Saglia et al. 1993, Mohr & Wegner 1997) and procedures applied to examine the ICM in smaller cluster samples (David et al. 1993, David, Jones & Forman 1995). The primary observational data required to study each cluster are (i) the X-ray surface brightness profile, which constrains the radial distribution of the ICM along with (ii) the X-ray luminosity within some aperture and (iii) the emission weighted mean ICM temperature $\langle T_X \rangle$, which together constrain the ICM central density. We demonstrate that our ICM constraints are insensitive to temperature variations within the cluster. Departing from some other published analyses, we do not assume a particular form for the dark matter distribution, because it is not necessary to do so when studying the ICM; however, we do assume a spherically symmetric ICM distribution. We test our technique on an ensemble of hydrodynamical cluster simulations and quantify the effects of present epoch mergers and asphericity on our results.

We describe the data and numerical simulations in §2, detail the analysis in §3, and then present the results in §4. Section 5 contains a discussion of the results. We use $H_0 = 50$ km/s/Mpc and $q_0 = \frac{1}{2}$ throughout.

2. DATA

We study members of an X-ray flux limited sample of 55 clusters (Edge et al. 1990) that were observed with the ROSAT PSPC. Archival PSPC images of forty-eight members exist, but Abell 399 lies partially outside the PSPC field of view (FOV), Virgo extends well beyond the PSPC FOV, and the quality of the short (850 s) exposure of Abell 2147 image is well below the others. Of the remaining 45 clusters, three have no upper limits on their temperature uncertainties, and so as noted later we exclude them from portions of the final analysis. The final sample is very similar to the same sample analyzed in a study of the X-ray Size-Temperature Relation (Mohr & Evrard 1997).

2.1. *X-ray Images*

We obtain the ROSAT data products on-line through the High Energy Astrophysics Science Archive Research Center (HEASARC), and we reduce these images using PROS and Snowden analysis software (Snowden et al. 1994). The X-ray image for each PSPC observation is the sum of individually flat fielded Snowden energy bands $R4$ through $R7$, corresponding approximately to the energy band 0.5–2.0 keV. We exclude time intervals with master veto rates higher than 220 cts/s, and exclude other high background time intervals whose inclusion would degrade the detection significance of a source 10% as bright as the background (Pildis, Bregman & Evrard 1995). We produce uncertainty images by assuming Poisson noise, estimating a 1% uncertainty in the flatfields, and applying standard error propagation. Multiple PSPC observations of the same cluster are registered and combined using the positions of bright point sources where possible, or, alternatively the image header pointing positions. We remove obvious point sources not coincident with the peak in the extended emission using the IRAF task *imedit*. The pixel scale is $14\farcs947$, and the effective angular resolution is FWHM$\sim 0\farcm75$. Table 1 contains a list of clusters and relevant information, including ROSAT sequence number(s) of observations incorporated into the final cluster image, effective exposure time t_{exp}, and the emission weighted mean ICM temperature $\langle T_X \rangle$.

The procedure described above produces images in units of photons per second; we use PROS software to convert to cgs flux units ergs/s/cm^2 in the restframe of the cluster. In the conversion we assume an isothermal ICM emitting a Raymond–Smith spectrum with 30% solar abundances and a temperature $\langle T_X \rangle$. We also correct for galactic absorption.

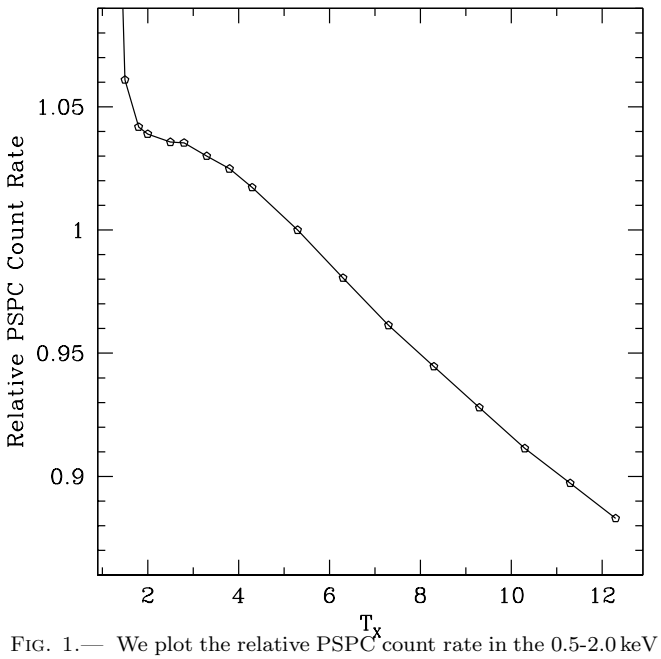

FIG. 1.— We plot the relative PSPC count rate in the 0.5-2.0 keV band for a parcel of gas with constant emission measure and varying temperature. The emission model is Raymond-Smith with 30% solar abundances. Note that for $T_X > 1.5$ keV a factor of two increase in temperature only decreases the PSPC count rate by ∼10%.

2.2. *ICM Temperatures*

We use published, emission weighted ICM temperatures $\langle T_X \rangle$ in our analysis (see Table 1). Approximately a third of these temperatures come from *Einstein* MPC observations, but where possible we have substituted more accurate measurements made with *Ginga* or ASCA observations. The sources for the temperature measurements include: *Einstein* MPC: David et al. 1993; *Ginga*: Day et al. 1991, Allen et al. 1992, Johnstone et al. 1992, David et al. 1993, Hughes et al. 1993, Arnaud & Evrard 1998; ASCA: Henriksen & Markevitch 1996, Markevitch 1996, Matsuzawa et al. 1996, Tamura et al 1996, Markevitch & Vikhlinin 1997, Markevitch et al. 1998.

2.3. *Hydrodynamical Cluster Simulations*

We use an ensemble of 48 hydrodynamical cluster simulations to better understand the systematics in the measurements presented below. The cluster simulations are carried out within four different cold dark matter (CDM) dominated cosmogonies (1) SCDM ($\Omega = 1$, $\sigma_8 = 0.6$, $h_{50} = 1$, $\Gamma = 0.5$), (2) τCDM($\Omega = 1$, $\sigma_8 = 0.6$, $h_{50} = 1$, $\Gamma = 0.24$), (3) OCDM ($\Omega_0 = 0.3$, $\sigma_8 = 1.0$, $h_{50} = 1.6$,

$\Gamma = 0.24$), and (4) LCDM ($\Omega_0 = 0.3$, $\lambda_0 = 0.7$, $\sigma_8 = 1.0$, $h_{50} = 1.6$, $\Gamma = 0.24$). Here σ_8 is the power spectrum normalization on $8h^{-1}$ Mpc scales; initial conditions are Gaussian random fields consistent with a CDM transfer function with the specified Γ (Davis et al. 1985). Within each of these models, we use two 128^3 N–body only simulations of cubic regions with scale ~ 400 Mpc to determine sites of cluster formation. Within these initial runs the virial regions of clusters with Coma–like masses of 10^{15} $M_\odot$ contain $\sim 10^3$ particles.

Using the N–body results for each model, we choose clusters for additional study. We zoom in on these clusters, resimulating them at higher resolution with gas dynamics and gravity on a 64^3 N–body grid. The large wavelength modes of the initial density field are sampled from the initial conditions of the large scale N–body simulations, and power on smaller scales is sampled from the appropriate CDM power spectrum. The simulation scheme is P3MSPH (Evrard 1988), the baryon density is a fixed fraction of the total $\Omega_b = 0.2\Omega_0$, and radiative cooling is ignored.

Simulating individual clusters requires two steps: (1) an initial, 32^3, purely N–body simulation to identify which portions of the initial density field lie within the cluster virial region at the present epoch, and (2) a final, effectively 64^3, three species, hydrodynamical simulation. In the final simulation the portion of the initial density field which ends up within the cluster virial region by the present epoch is represented using dark matter and gas particles of equal number, while the portions of the initial density field that do not end up within the cluster virial region by the present epoch are represented using a third, collisionless, high mass, species. The high mass species is 8 times more massive than the dark matter particles in the central, high resolution region. This approach allows us to include the tidal effects of the surrounding large scale structure and the gas dynamics of the cluster virial region with simulations that take only a few days of CPU time on a low end UltraSparc. The scale of the simulated region surrounding each cluster is in the range 50–100 Mpc, and varies as $M_{halo}^{1/3}$, where M_{halo} is approximately the mass enclosed within the present epoch turn around radius. Thus, the 48 simulated clusters in our final sample have similar fractional mass resolution; the spatial resolution varies from 125–250 kpc. The masses of the final cluster sample vary by an order of magnitude. We create X–ray images and temperature maps for further analysis following procedures described in Evrard (1990).

3. ANALYSIS

In this section, we detail our data reduction procedures, placing special emphasis on the determination of statistical uncertainties and systematic errors in the derived cluster ICM gas masses.

3.1. *Modeling the X-ray Surface Brightness Profile*

We use the reduced, cluster X–ray images to constrain the underlying ICM distribution. Our approach is to fit radial surface brightness profiles of the cluster emission to the standard β model (Cavaliere & Fusco–Femiano 1978) of the form

$$I(R) = I_0 \left[1 + \left(\frac{R}{R_c}\right)^2\right]^{-3\beta+\frac{1}{2}} \quad (1)$$

where R_c is the core radius and $r^{-3\beta}$ is the asymptotic radial fall-off of the underlying ICM density distribution. Because the PSPC photon detection rate for a parcel of gas with constant emission measure varies only moderately with temperature above 1.5 keV (see Fig. 2.1), the distribution of X–ray photons in PSPC images directly constrains the ICM density distribution regardless of the temperature structure (see similar discussion of the *Einstein* IPC: Fabricant, Lecar & Gorenstein 1980). Fitting the β model provides a systematic approach to studying the ICM properties. In the case where cluster X–ray emission is well described by β models — even flattened β–models with axial ratios within the observed range (Mohr et al. 1995) — fitting to azimuthally averaged surface brightness profiles recovers unbiased estimators of β and R_c as long as the point source response function (PSF) of the imager is properly treated.

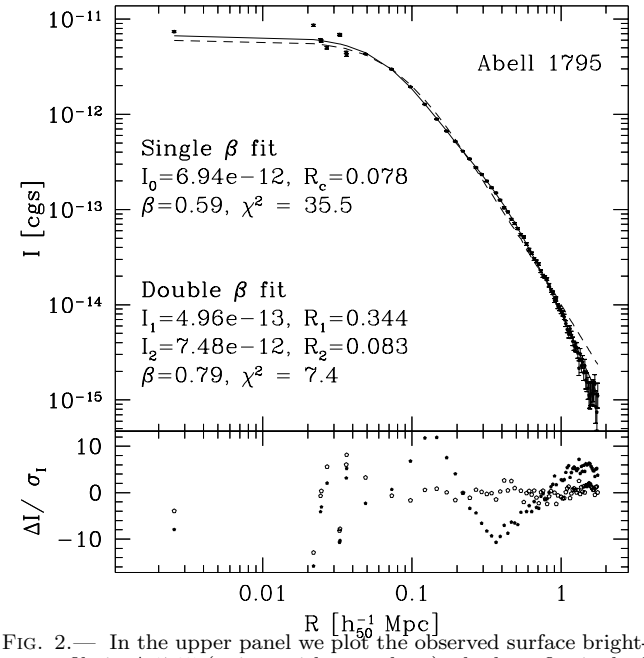

FIG. 2.— In the upper panel we plot the observed surface brightness profile in A 1795 (points with error bars), the best fit single β model (dashed line), and the best fit double β model (solid line). The lower panel contains residuals around the single β (solid) and the double β (open) fits. In clusters with central emission excesses, a single β fit produces an artificially small core radius and β; adding the second β component results in an improved fit to the emission excess and the outer profile.

Unfortunately, approximately half of nearby galaxy clusters exhibit X–ray emission which is not azimuthally symmetric (Mohr, Fabricant & Geller 1993, Mohr et al. 1995). These features include large centroid variations (e.g. A 754) and bimodality (e.g. A 85) which violate the assumptions underlying Eqn. 1. Nevertheless, we find that the β model describes azimuthally averaged cluster emission reasonably well and produces sensible results for most clusters. As discussed in detail below (§3.6), we quantify the systematics associated with β model fitting to radial profiles by analysing an ensemble of simulated clusters that

exhibit X–ray morphologies similar to those of our PSPC cluster sample.

The presence of cooling flows presents another potential problem to our choice of model. Significant central emission excesses associated with cooling instabilities are found in 18 of the clusters in our sample; they can greatly bias the model parameters. Clusters for which cooling flows present a problem to fitting are easily recognized by two criteria. First, the cluster must display nonrandom behaviour in the fit residuals consistent with a central emission excess. Second, the cluster must appear "relaxed", lacking obvious asphericity or substructure which would indicate a recent merger. Figure 3.1 shows an example of these criteria in Abell 1795, a symmetric cluster which displays a significant central emission excess. The emission excess biases our best-fit β model (the dashed line) towards a small core radius and shallow profile, resulting in poor agreement between fit and data in the region outside the excess.

In such cases we model the emission excess with a second β model and simply fit the cluster surface brightness profile to the sum of the two:

$$I_D(R) = \sum_{i=1}^{2} I_i \left[1 + \left(\frac{R}{R_i}\right)^2\right]^{-3\beta+\frac{1}{2}}. \qquad (2)$$

We constrain both components of this function to have the same β, and we determine the distribution of the underlying ICM numerically. This method essentially decouples the inner and outer regions of the cluster, allowing the fit to find the transition between excess and primary emission on its own. An example of a two-component fit is also shown in Figure 3.1 (solid line); the extra degrees of freedom are effective in removing nonrandom trends from the residuals. In the process of formulating our method, we also considered removing the emission excess and fitting a single component β model to the remainder of the image. We found that fitting under these conditions produces biased parameter estimates in cases where the emission model *is* a perfect β model; specifically, the best fit core radius is correlated with the size of the excised region. These systematics and associated signal to noise reductions led us to abandon this approach. The double β model approach is similar in spirit to this method and usually gives similar results, but is much more objective.

3.2. *Calculating Radial Profiles*

Producing a background subtracted cluster surface brightness profile appropriate for fitting requires several steps. First, we choose an emission center using a circular aperture of radius 10 pixels. We adjust the position of this aperture to minimize the difference between the geometric center and the centroid of the X-ray photon distribution which lies within the aperture. This approach converges even in cases where the cluster emission is significantly skew (Mohr, Fabricant & Geller 1993).

Second, we evaluate the background level in the image by examining annuli at large radii where the cluster surface brightness makes a negligible contribution. Specifically, we measure the background surface brightness within 5 concentric, overlapping annuli with 20 pixel width and inner radii ranging from 140 to 180 pixels. The background value for each annulus is the mean of the clipped distribution of the $\sim 2\times10^4$ pixels within the annulus. The clipping algorithm excludes all pixels that are more than $2\sigma_i$ brighter than the median value, where σ_i is the uncertainty associated with pixel i. The clipping algorithm is iterated 10 times, with upper and lower sigma clipping during the last two iterations. Tests on simulated PSPC images indicate that the mean value is an unbiased estimator of the image background.

This method allows us to detect clusters whose emission contaminates the entire image, by seeing whether the background values steadily decrease with increasing radius. It also guards against the possibility of localized excess emission contaminating our result. In cases where the neighboring clusters contaminate the image background region in one direction (e.g. A 3558), we use half rather than full annuli. In the end, we measure the background in the annulus whose background value lies closest to the mean of the five measurements; in cases where detectable cluster emission essentially fills the PSPC FOV, we use the background value in the outermost annulus. We use the scatter in the five background measurements as an indicator of the true background uncertainty.

Lastly, we calculate the radial profile. Individual pixels are treated separately within 1.5 pixels of the image centroid; outside this region the profile values are averages over all pixels whose centers lie within an annulus of 1 pixel width. The profile is truncated at the radius θ_{max} where the signal to noise falls below a critical value; specifically, the profile is terminated when the average signal to noise of the last few profile points falls below ~ 3. A few clusters are treated differently because of contamination by neighboring clusters; for example, Abell 401 is fit out to a radius halfway between it and Abell 399.

3.3. *Fitting β Models*

We find the best estimates of the parameters I_0, β, and R_c by minimizing the χ^2 difference between the PSF convolved model and the observed surface brightness profile. We minimize χ^2 using the downhill simplex method (Press et al. 1992). In correcting for the effects of the PSF and finite pixel scale we employ the techniques used in studies of the fundamental plane of elliptical galaxies (Saglia et al. 1993, Mohr & Wegner 1997). The PSF convolved mean surface brightness I_c within an annulus of radius R and width $2dR$ is

$$I_c(R) = \frac{[F(R+dR) - F(R-dR)]}{4\pi R dR} \qquad (3)$$

where $F(R)$ is the integrated flux contained within a radius R. The integrated flux is a function of the β model parameters and the PSF.

$$F(R) = R\int_0^\infty dk J_1(kR)\hat{p}(k)\hat{I}(k) \qquad (4)$$

where J_1 is the Bessel function and $\hat{p}(k)$ and $\hat{I}(k)$ are the Fourier transforms of the PSF and the one or two component β model. We use a PSF of the form

$$\hat{p}(k) = e^{-(kb)^\gamma} \qquad (5)$$

where the two free parameters b and γ describe the scale and shape of the PSF. We determine the best fit PSF parameters $b = 0.47$ and $\gamma = 1.89$ by fitting to artificial point

sources created with the PROS task *rosprf* at 1.0 keV (see Fig. 3.3); these parameters are appropriate for the central part of the PSPC field, consistent with the position of cluster cores in this dataset.

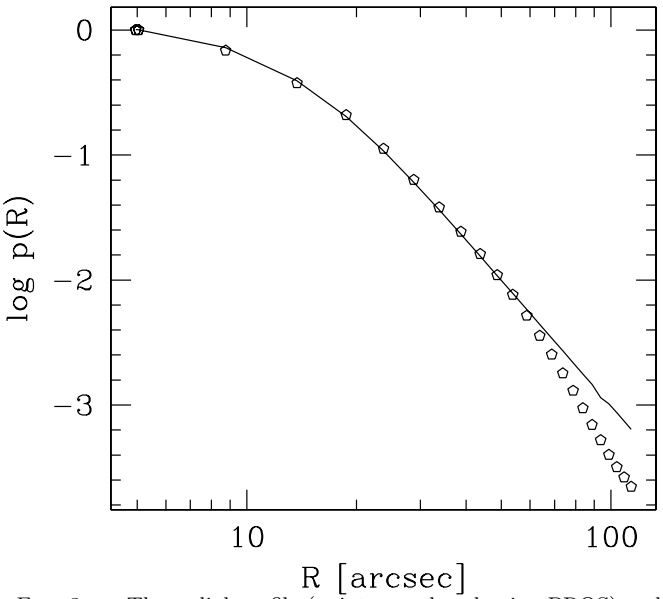

FIG. 3.— The radial profile (points; produced using PROS) and fit (solid line; see Eqn. 5) of a 1 keV point source located in the center of the ROSAT PSPC field. The divergence of the model and the true PSF at radii greater than 60″ does not bias estimates of β model parameters.

The Fourier transform of the one component β model $I(R)$ is

$$\hat{I}(k) = 2\pi I_0 R_c^2 \int_0^\infty d\lambda \frac{\lambda J_0(kR_c\lambda)}{(1+\lambda^2)^{-3\beta+\frac{1}{2}}} \qquad (6)$$

where J_0 is the Bessel function. This function $\hat{I}(k)$ is not analytic for all β, but note that the integral is only a function of β and the combination kR_c. Our approach is to calculate $\hat{I}(k)$ over a finely sampled grid in β and kR_c and then interpolate on this grid when evaluating the PSF convolved surface brightness $I_c(R)$ (Eqn. 3). We test the accuracy of this grid by comparing the inverse transform of $\hat{I}(k)$ directly with $I(R)$. The Fourier transform of the two component β model is simply the sum of the transforms of the individual components. Naturally, the PSF corrected surface brightness $I_c(R)$ approaches the uncorrected profile $I(R)$ at radii which are several times the PSF scale, so at large radii we use the unconvolved surface brightness $I(R)$ (Eqn. 1) directly.

3.4. *Calculating ICM Masses*

We constrain the ICM central density using the cluster X–ray luminosity measured within an annulus (e.g. David et al. 1990, Mohr et al. 1996). Specifically, the luminosity within an annulus defined by a minimum radius R_- and a maximum radius R_+ is

$$L_X(R_-, R_+) = 4\pi \int_0^\infty dz \int_{R_-}^{R_+} n_e(r) n_H(r) \Lambda(T) R dR \quad (7)$$

where $n_e(r)$ and $n_H(r)$ are the electron and proton number densities, $\Lambda(T)$ is the radiative cooling coefficient and $r^2 = R^2 + z^2$. The integral along z can be truncated at the cluster "boundary"; tests demonstrate that for observed values of β this integral is not sensitive to its upper limit. Using $n_e(r) = \rho(r)/\mu_e m_p$ and $n_H(r) = \rho(r)/\mu_H m_p$ the ICM central density is

$$\rho_0 = \left(\frac{L_X(R_-, R_+)\mu_e \mu_H m_p^2 (1-3\beta)}{2\pi\Lambda(\langle T_X \rangle) R_c^3 F(R_-, R_+)} \right)^{\frac{1}{2}} \qquad (8)$$

where $F(R_-, R_+)$ is the dimensionless integral

$$F(R_-, R_+) = \int_0^\infty ds \left[\left(1 + s^2 + (R_+/R_c)^2\right)^{1-3\beta} - \left(1 + s^2 + (R_-/R_c)^2\right)^{1-3\beta} \right], \qquad (9)$$

and we have assumed that the ICM is isothermal with temperature $\langle T_X \rangle$. For the results presented here we measure the luminosity over the same region we fit the X-ray surface brightness profile ($R_- = 0$ and $R_+ = \theta_{max}$).

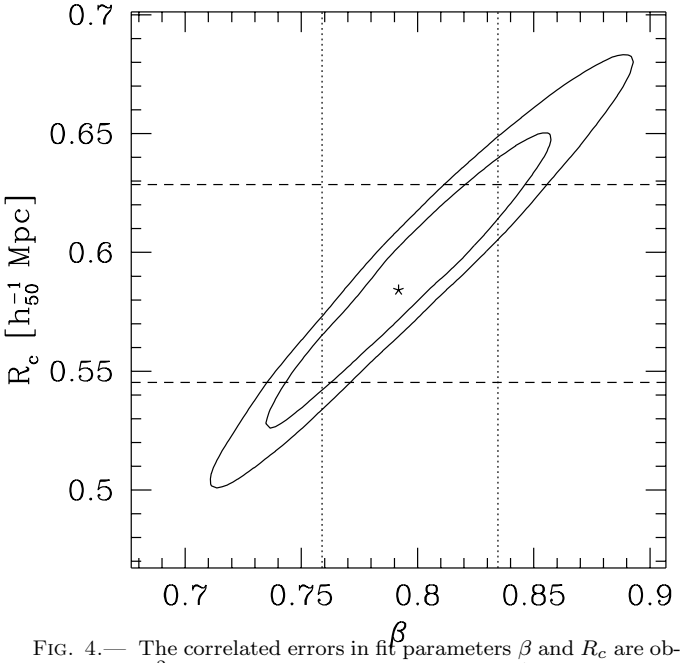

FIG. 4.— The correlated errors in fit parameters β and R_c are obvious in this χ^2_ν contour plot. The best fit value for A 2255 is marked with a star, the contours deliniate 2σ and 3σ confidence regions, and the dotted and dashed lines correspond to 90% confidence intervals determined by Monte Carlo runs. The uncertainties presented with tabulated results are derived from Monte Carlo simulations.

In determining ρ_0 we use $\mu_e = 1.167$ and $\mu_H = 1.400$, appropriate for a fully ionized plasma with 30% solar abundances (Feldman 1992). The ICM mass within some limiting radius is then a straightforward integral over the β model density distribution using the measured ICM central density (Eqn. 8).

The density distribution consistent with a two component β model is not analytic in general. We express the density distribution in the two component case as a radially dependendent multiple $f(r)$ of the broad, primary component: $\rho_D(r) = f(r)\rho_1(r)$; we solve for $f(r)$ using the surface brightness profiles of the two component fit $I_D(R)$ as a constraint:

$$I_D(R) = 2\frac{\Lambda(\langle T \rangle)}{\mu_e \mu_H m_p^2} \int_R^\infty \frac{r dr}{\sqrt{r^2 - R^2}} f^2(r) \rho_1^2(r) \qquad (10)$$

Using this equation, we work our way inward solving for $f(r)$ at equal intervals in r. The central density in this case is $\rho_0 = f(r)\rho_1(r)|_{r=0}$. In our sample the central value of the multiple $f(r=0)$ ranges from 2.5 (Ophiuchus) to 33 (A 2204) and averages $\sim$10.

3.5. *Measurement Uncertainties*

A uniform, systematic analysis of the ICM properties in this well defined cluster sample requires careful quantification of all known sources of uncertainty. We identify multiple sources of uncertainty in the measured properties of the ICM, including Poisson noise, choice of cluster emission center, PSF blurring, X–ray background subtraction, ICM temperature uncertainties, luminosity uncertainties, and $\langle T_X \rangle < 1.5$ keV gas associated with central cooling instabilities. Below we discuss each in turn, and describe how they are incorporated into the final uncertainties for the β model parameters and ICM masses M_{ICM}. We also quantify the impact of each error contribution on the derived ICM mass, to give some indication of their relative importance.

- *Poisson noise*: We evaluate the Poisson contribution to the uncertainties using a Monte Carlo approach. Specifically, we create and fit 500 independent realizations of each cluster image. The template for these artificial images is a Gaussian smoothed ($\sigma = 30''$) version of the original cluster image. Each pixel in an artificial image contains a value Poisson distributed around the mean of the pixel value in the template image. When fitting β models to the artificial images, we adjust the PSF parameters to account for the degraded resolution in the smoothed template. This approach allows us to account for the deviations of many clusters from idealized β models. We use this ensemble of 500 fits for each cluster to quantify the Poisson contribution to measurement uncertainties. The typical Poisson contribution to the fractional uncertainty in M_{ICM} is 1.1% (sample median), and the largest is 3.9% in A 1689.

  The fit parameters R_c and β are strongly correlated. In Fig. 3.4 we present 2σ and 3σ χ^2_ν contours in the space of R_c and β for the single component fit to the cluster A 2255. Rather than present these plots for each cluster we note the upper and lower 90% confidence intervals on the best fit parameters. Dashed lines indicate the locations of these confidence boundaries in Fig. 3.4.

- *Emission center*: We use a circular aperture with $150''$ radius to define the cluster emission center (see §3.2) before calculating the radial profile. In clusters with azimuthally symmetric emission, the emission center is independent of the aperture radius. In clusters that exhibit centroid variations this is not the case. Calculating the profile around different emission centers can affect core radii, β's and ICM masses. We evaluate these effects by re-analyzing the cluster images using a centering aperture three times larger. We find that the measured properties of the ICM are insensitive to centering aperture radius except for those few clusters with grossly asymmetric X-ray images. The substructure in these clusters indicates recent major mergers, and, for the most part, they can be identified by the high χ^2_ν in the fit results. We use the difference in ICM parameters in the two different analyses as an estimate of the scale of this uncertainty. The ratio of M_{ICM} measurements with the two centering apertures has a mean value of 0.997 and a standard deviation of 2.5% calculated over the whole sample; the largest outlier is A 754, a well studied recent merger candidate (e.g. Fabricant et al. 1986, Henriksen & Markevitch 1996, Roettiger, Stone & Mushotzky 1998), where M_{ICM} changes by 16%.

- *PSF correction*: Without a PSF correction, core radii and β's in small core radius clusters would be systematically overestimated. By fitting PSF corrected β models to observed radial profiles, we remove this bias from our β parameters and ICM masses. We ignore any residual errors associated with the minor differences between the true PSPC PSF and our best fit model (see Fig. 3.3).

- *X–ray background*: Errors in the background subtraction can systematically bias β parameters and X-ray luminosities. We use the variation in the measured background within five concentric annuli as a measure of the true background uncertainty σ_{XB} (see primary discussion in §3.1). We quantify the effects of the background uncertainty on measured ICM parameters by refitting the image with the background fixed to the preferred value perturbed by $\pm 1\sigma_{XB}$ and $\pm 2\sigma_{XB}$. For each cluster we use the five fits to measure a maximal deviation in the parameters of interest (corresponding to a $\sim 4\sigma_{XB}$ variation in the X-ray background); we use half this maximal difference as an estimate of the X-ray background induced uncertainty. In our ensemble, the RMS maximal deviation in $M_{ICM}$is 3.6%, and the largest change is 14% in MKW 3S.

- *ICM $\langle T_X \rangle$ measurements*: Typical measurement uncertainties in $\langle T_X \rangle$ translate into negligible uncertainties in the ICM parameters, but make important contributions to uncertainties in binding mass estimates. Eqn 8 shows that $\rho_0 \propto \sqrt{L_X/\Lambda}$ where L_X is the X-ray luminosity and Λ is the cooling coefficient. The temperature dependence of L_X and Λ is approximately the same, because to determine Ł$_X$ we measure the cluster X-ray count rate in the PSPC and then use an ICM emission model Λ, galactic absorption, cluster distance and the PSPC effective area tables to convert to a bolometric luminosity (PROS tasks). We quantify this effect by varying the temperature of the cluster A 1795 ($\langle T_X \rangle = 5.3$ keV) from 1 to 10 keV and calculating the resulting variations in ρ_0. Above 5 keV $\delta\rho_0 \sim \delta T_X^{0.055}$, so a factor of two increase in $\langle T_X \rangle$ corresponds to a $\sim 4\%$ increase in ρ_0; between 1 keV and 5 keV uncertainties in $\langle T_X \rangle$ have an even smaller effect on ρ_0.

  Temperature uncertainties dominate the formal uncertainties in the binding mass. We account for these uncertainties in measurements of M_{ICM} and f_{ICM}; note that M_{ICM} measured within a constant

$1h_{50}^{-1}$ Mpc aperture is unaffected by $\langle T_X \rangle$ uncertainties.

- *Luminosity measurements*: We measure cluster aperture luminosities using the PSPC images. With Eqn. 8 and the uncertainty in the observed cluster count rate, we calculate the contribution to uncertainties in the ICM parameters. The typical contribution to M_{ICM} uncertainties is 0.4% (sample median) and the largest contribution is 1% in A 2244. We do not account for any errors in the PSPC effective area tables; upcoming observations with AXAF will provide an excellent test of these data.

- *Core ICM with $T_X < 1.5$ keV*: The PSPC count rate for a parcel of gas with constant emission measure is relatively insensitive to T_X for $T_X > 1.5$ keV (see Fig. 2.1); therefore, our assumption of isothermality when we calculate the underlying density profile consistent with the X-ray surface brightness profile does not affect our results. However, ICM temperatures within the cores of clusters which exhibit strong emission excesses or cooling flows can be less than 1.5 keV. In clusters where this is the case the ICM in the cores is essentially overrepresented with photons in the cluster X-ray image. Specifically, the PSPC count rate for a 1 keV (0.75 keV) gas clump is $\sim$1.4 ($\sim$ 2) times higher than the count rate for a 5 keV gas clump.

  In the absence of detailed ICM temperature profiles, we estimate the effects of these cool cores empirically. We use the clusters with two component β model fits to estimate the nature of this effect on M_{ICM} measurements. Specifically, we assume that the secondary component of the fit is responding to ICM at a temperature of 0.75 keV; thus, we scale the best fit I_2 by $\frac{1}{2}$ to account for the factor of two higher PSPC count rate, and then recalculate the ICM distribution and M_{ICM}, taking care to account for the change in the cluster aperture luminosity. Results indicate that our standard isothermal analysis overestimates the true M_{ICM} in this case; in our sample of 18 clusters with double β model fits, M_{ICM} is overestimated by $\sim$ 3.5% on average, with a maximal overestimate of 14% in A 2204. The ICM radial distribution is less affected: $\langle r \rangle / r_{500}$ is underestimated by less than 1%.

  We emphasize that the toy model presented here overestimates the effects of cool gas on M_{ICM} measurements, because we have assumed that cool gas extends throughout the cluster (traced by the secondary β component), whereas the cool gas is likely confined to the core regions where the cooling time falls well below the Hubble time.

We combine these sources of uncertainty as follows. First, these different error terms are independent of one another and we assume that they are each Gaussian distributed; we combine all but the Poisson contribution in quadrature and call it σ_{NP}. Second, we convolve the 500 Monte Carlo results for each cluster with a Gaussian of scale σ_{NP}, and integrate over the distribution to calculate the 90% confidence intervals. These confidence intervals appear with the results.

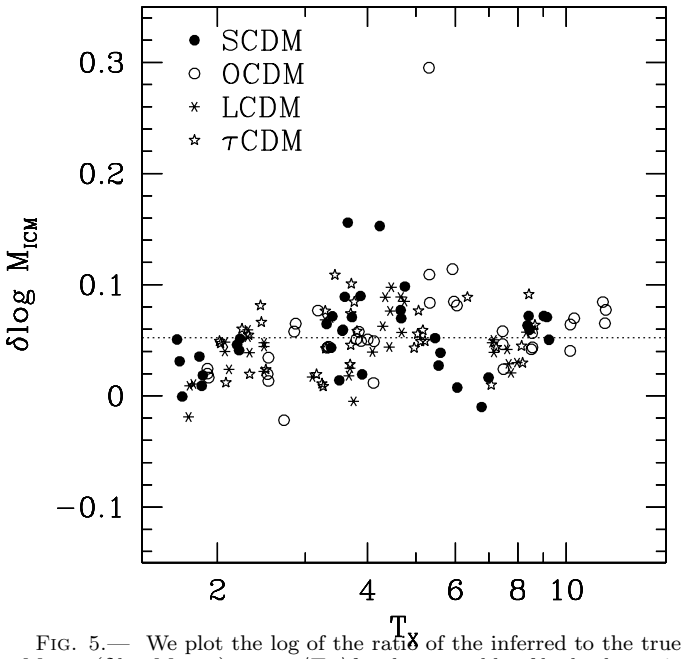

FIG. 5.— We plot the log of the ratio of the inferred to the true M_{ICM} ($\delta \log M_{ICM}$) versus $\langle T_X \rangle$for the ensemble of hydrodynamic simulations. Estimates of M_{ICM} lie systematically higher than the true values; the dotted line shows the median overestimate of 12% for the set of 144 images.

3.6. *Testing Our Technique with Simulated Clusters*

We test the accuracy of our ICM measurements using an ensemble of 48 hydrodynamical cluster simulations (discussed in §2.3). The simulations allow us to examine the effects of (i) departures of the true ICM density distribution from the β model and (ii) ICM temperature variations within the cluster. The simulated clusters experience present epoch mergers consistent with expectations for their CDM cosmogonies; X-ray morphologies of the simulated clusters in three of the four cosmological models are statistically consistent with the X-ray morphologies of the PSPC cluster sample, with the τCDM simulations exhibiting somewhat more substructure than observed clusters (Mohr & Evrard, in prep). We analyze images of these simulated clusters as though they were true cluster images and then compare the estimates of the ICM mass fraction to the real values.

Interestingly, we overestimate the true ICM masses; the median overestimate for a sample of 144 images is 12%, and the RMS scatter around this median is $\sim$ 9% (see Fig. 3.5). This bias arises because the ICM distribution in simulated clusters is not perfectly described by an isotropic, smooth density function. ICM density fluctuations around the mean value at a given radius enhance the X-ray emissivity of the gas which is proportional to the square of the density. We examine the ICM distribution in the simulations and measure the quantity $\delta_{ICM} = \langle \rho \rangle / \sqrt{\langle \rho^2 \rangle} - 1$ where ρ is the local ICM density; because the ICM emissivity ϵ_X scales as $\epsilon_X \propto \rho^2$, the overestimate in M_{ICM} scales linearly with δ_{ICM}. We find that within r_{500} the fluctuation amplitude is $\delta_{ICM} \sim 13\%$, in good agreement with the median overestimate in M_{ICM}.

These density fluctuations are presumably residual structure in the ICM from recent mergers; higher resolution simulations would likely yield even higher fluctuation amplitudes. We are carrying out a detailed analysis of the ICM structure in our simulated ensemble to better characterize the source of these density fluctuations (Mathiesen, Evrard & Mohr in prep). In real clusters this mechanism and additional physics like magnetic fields and radiative cooling instabilities (all explicitly ignored in these simulations) could all contribute to ICM density fluctuations (and overestimates of M_{ICM}). Quantifying the M_{ICM} measurement biases in real clusters requires detailed analysis of high resolution, spatially resolved, X-ray spectra of the ICM emission or comparison of M_{ICM} measurements from X-ray data and observations of the ICM's Sunyaev-Zeldovich effect on the cosmic microwave background.

In summary, our ensemble of hydrodynamical cluster simulations indicates that (i) our analysis technique is likely to overestimate M_{ICM}, and (ii) (after accounting for this bias) high signal to noise X-ray images of a coeval cluster population allow the determination of M_{ICM} with a typical accuracy of $\sim 9\%$.

4. RESULTS

Below we present results of an analysis of our X-ray flux limited sample of 45 galaxy clusters. First we describe our analysis of the cluster X-ray surface brightness profiles. Second, we present our constraints on ICM masses M_{ICM} and mass fractions f_{ICM}, and third, we constrain systematic variations in the radial distribution of the ICM. Finally, we compare our results to previously published analyses.

4.1. *X-ray Surface Brightness Profiles*

Best fit parameters for the profiles appear in Table 2. Columns contain the cluster name, the central surface brightness and core radius of the primary β model component, the central surface brightness and core radius of the secondary component (if there is one), the best fit β, the reduced χ^2_ν, the number of constraints in the fit, and the truncation radius of the fit θ_m (we also measure our aperture luminosities within θ_m). Central surface brightnesses are the unabsorbed values in ergs/s/cm^2/$\Box'$ for the 0.5-2.0 keV band. Core radii are in h_{50}^{-1} Mpc (with $q_0 = 0.5$), and the truncation radii θ_m are in arcminutes. Uncertainties are 90% confidence intervals with the other fit parameters unconstrained.

The X-ray surface brightness profile of each cluster appears in Fig. 6. Each page contains a two by three arrangement of cluster panels. The clusters are arranged by $\langle T_X \rangle$, which facilitates the fixed radial range for each group of six. Cluster names appear in the upper right corner of each panel. Surface brightness (in ergs/s/cm^2/$\Box'$ in the 0.5-2.0 keV band) is plotted versus radius in h_{50}^{-1} Mpc. We plot measurements (points with error bars), best fit profile (solid line), and best fit profile without the PSF correction (dashed line) for each cluster. The best fit parameters appear below the cluster name. The fit residuals are at the bottom of each panel. An X-ray contour plot is located at the lower left of each panel; contours are of a smoothed version of the portion of the X-ray image used to calculate the surface brightness profile. Contours appear at factors of 2.5 in surface brightness, and the heavy contour always corresponds to 4×10^{-14} ergs/s/cm^2/$\Box'$.

We fit two component β models to 18 clusters in our sample; these clusters exhibit trends in the residuals of their fits to single component β models. Some remaining clusters with single component β fits exhibit trends, but these clusters also exhibit large centroid variations or other evidence of recent mergers, and so we do not attempt a double component fit: (A 754, A 1367, A 2319, A 3266, A 3558, A 3667). Two clusters with double component fits also exhibit obvious evidence of recent mergers: A 2142 and A 85; in the case of A 85 we remove the small, secondary surface brightness peak to the south before calculating a radial profile.

It is interesting to note that 29 clusters in our sample are not formally well fit by either a one or two component β model (less than 1% chance of consistency between model and data). This is most likely another indicator of the prevalence of cluster X-ray substructure (Mohr et al. 1995). However, in all but a few clusters the best fit β model reproduces the general character of the surface brightness profile (no systematic trends in the residuals), and, as demonstrated by our analysis of the cluster simulations, this is all that is required to constrain the average behavior of the density profile and calculate M_{ICM} with a typical accuracy of $\sim$9%. (Note that parameter uncertainties are determined using Monte Carlo simulations and not $\Delta\chi^2$.)

Note that the high χ^2_ν fitting problem for galaxy clusters is similar to that of elliptical galaxies. Elliptical galaxies are reasonably well described by bulge plus disk models, but very rarely are the measured galaxy profiles and models consistent in a formal χ^2 sense (Saglia et al. 1997); interestingly, the photometric parameters derived from those fits exhibit the fascinating regularity relation termed the Fundamental Plane.

4.2. *ICM Properties*

We use the fit to the X-ray surface brightness profile of each cluster to constrain the ICM central density, radial distribution, and total mass within several limiting radii r_{lim}. We use $r_{lim} = 1h_{50}^{-1}$ Mpc and $r_{lim} = r_{500}$, the radius within which the mean density is 500 times the critical density $\rho_{crit} = 3H_0^2/8\pi G$. By using r_{500} we are able to study the same portion of the virial region in each cluster; a drawback is that one requires a model of the potential to calculate r_{500}, and so we also present measurements within a fixed metric radius to avoid this uncertainty. We calculate the radius r_{500} and enclosed binding mass M_{500} two different ways: (i) using virial scaling relations and (ii) using the isothermal β model. The virial scaling relation is motivated by the simple assumptions that clusters have recently formed and are approximately virialized and self-similar; in this case $r_{500} \propto T^{1/2}$ and $M_{500} \propto T^{3/2}$. Our simulated cluster ensemble exhibits scaling relations consistent with these assumptions, in agreement with previous work (Evrard, Metzler & Navarro 1996, Schindler 1996). On the other hand, estimates of M_{500} and r_{500} with the β model require only that the ICM be approximately in hydrostatic equilibrium. Rather than using simulated clusters to normalize our scaling relation, we normalize using the β model results in the relatively relaxed cluster

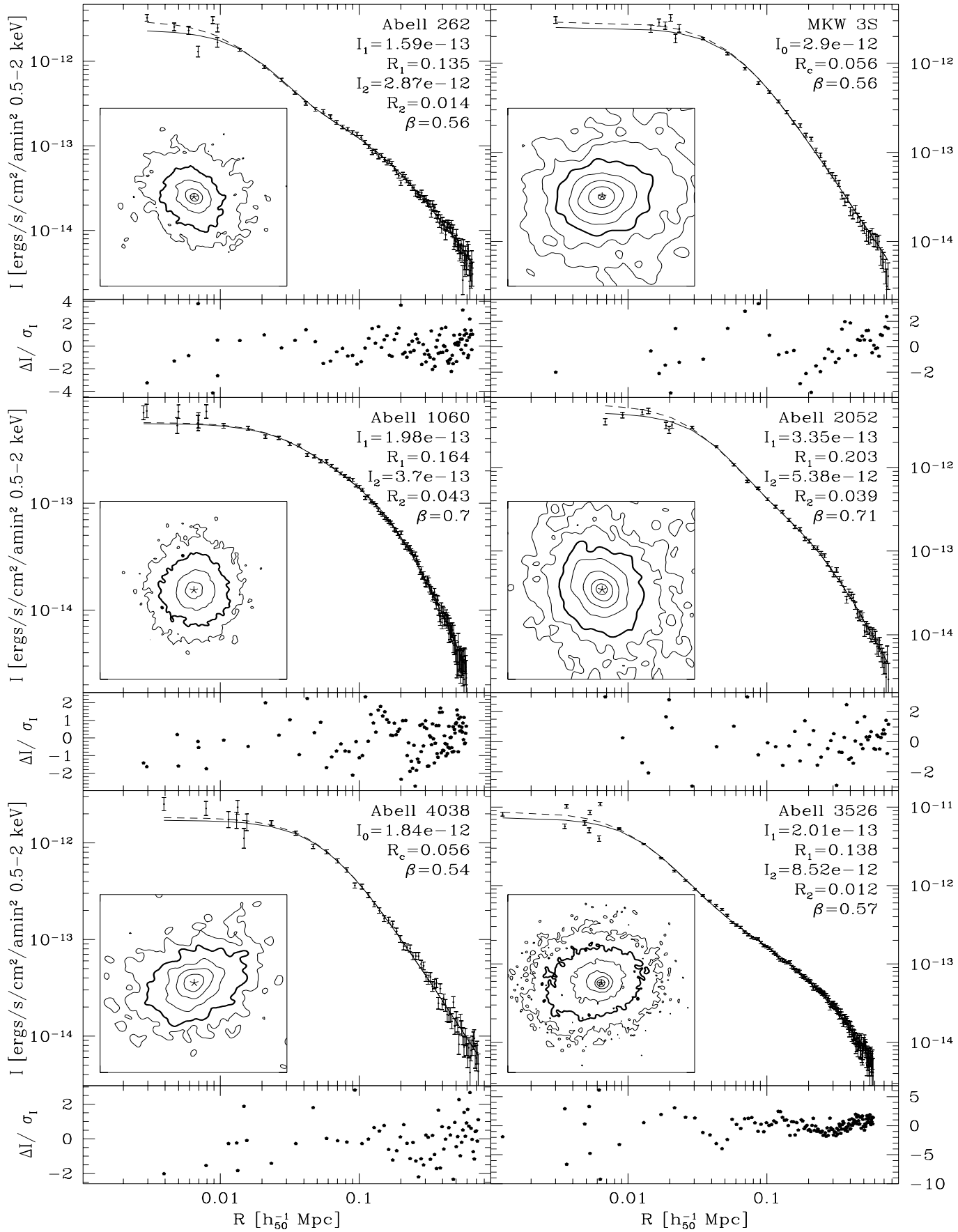

FIG. 6.— A 262, MKW 3S, A 1060, A 2052, A 4038, A 3526

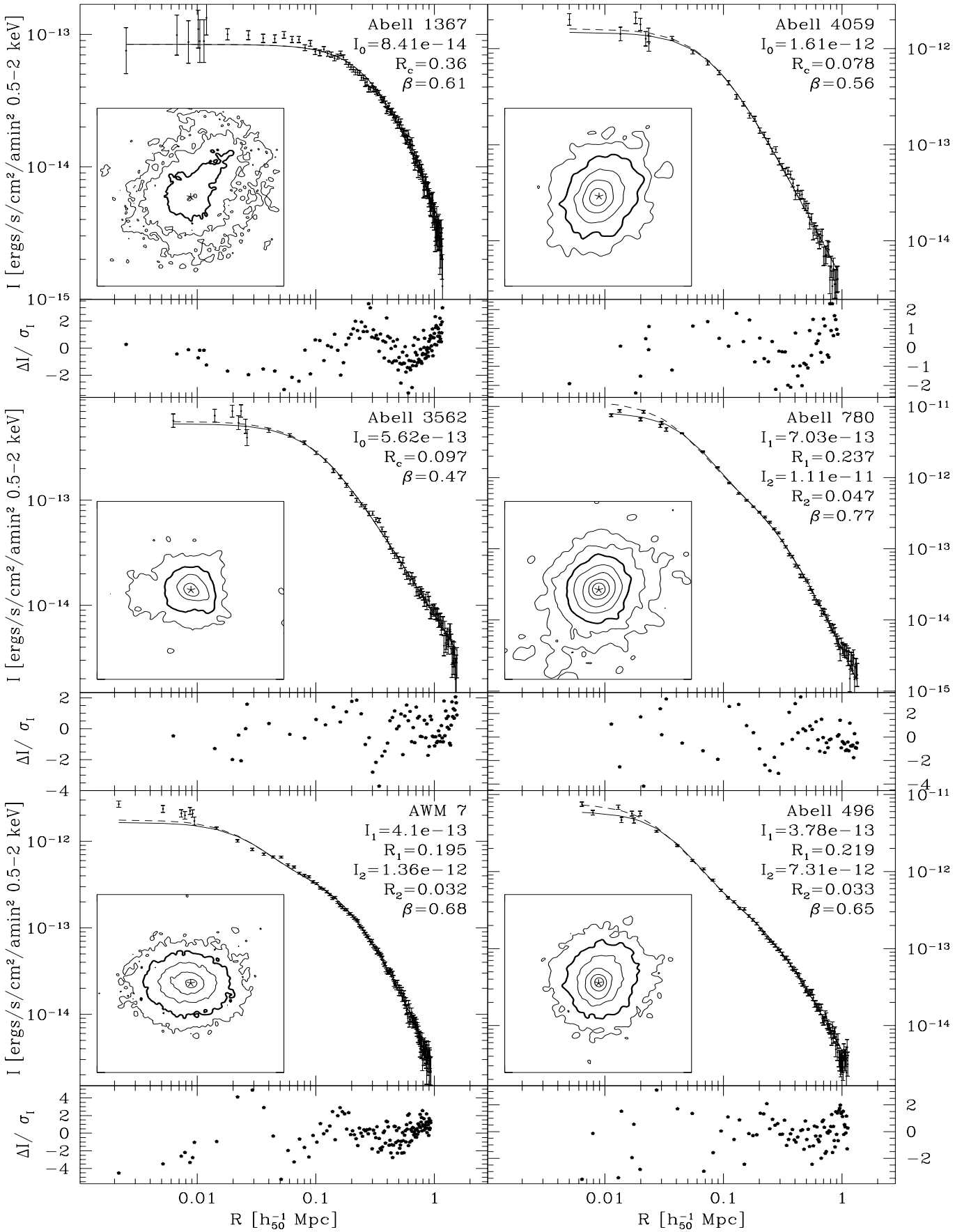

FIG. 6B.— A 1367, A 4059, A 3562, A 780, AWM 7, A 496

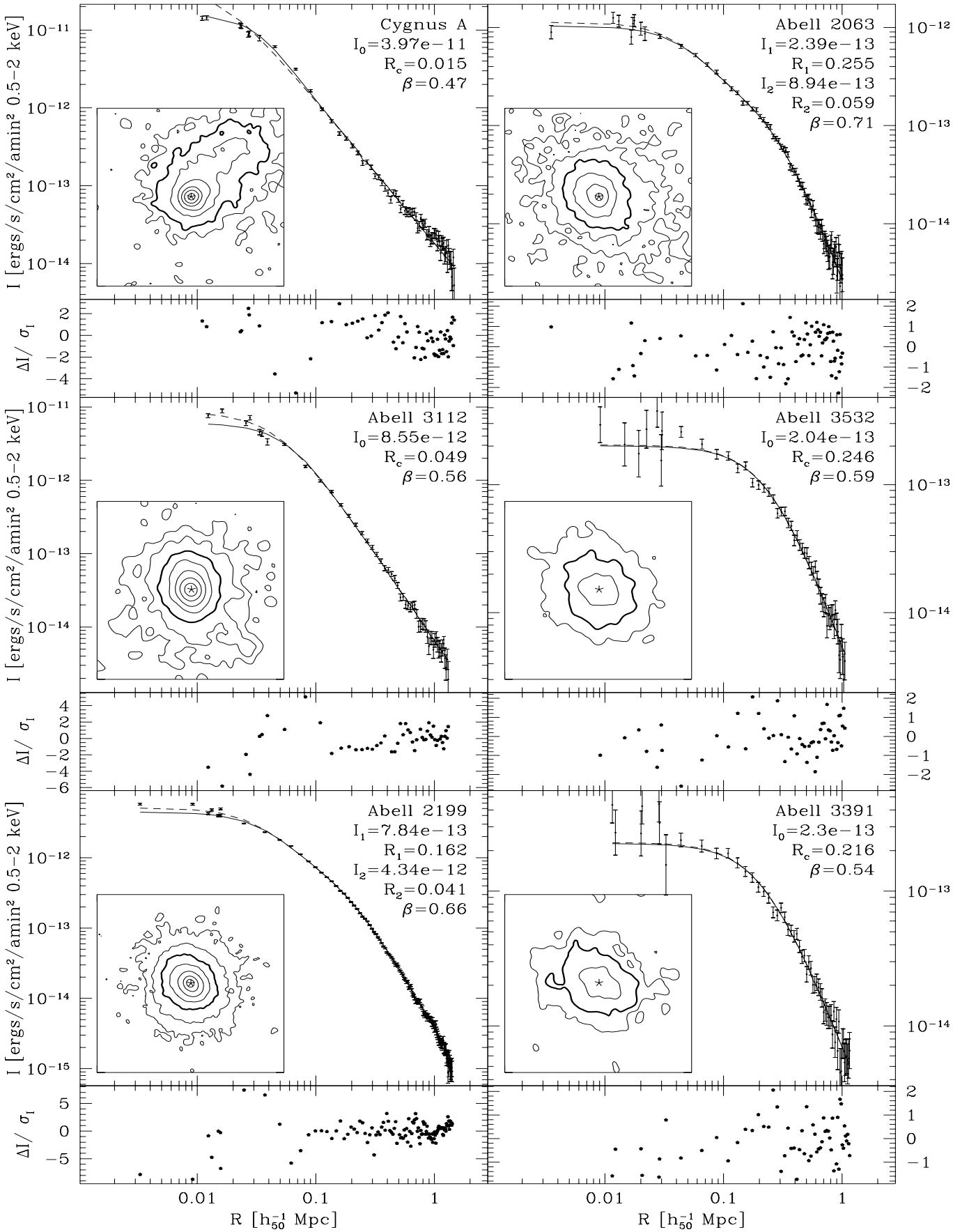

FIG. 6c.— Cygnus A, A 2063, A 3112, A 3532, A 2199, A 3391

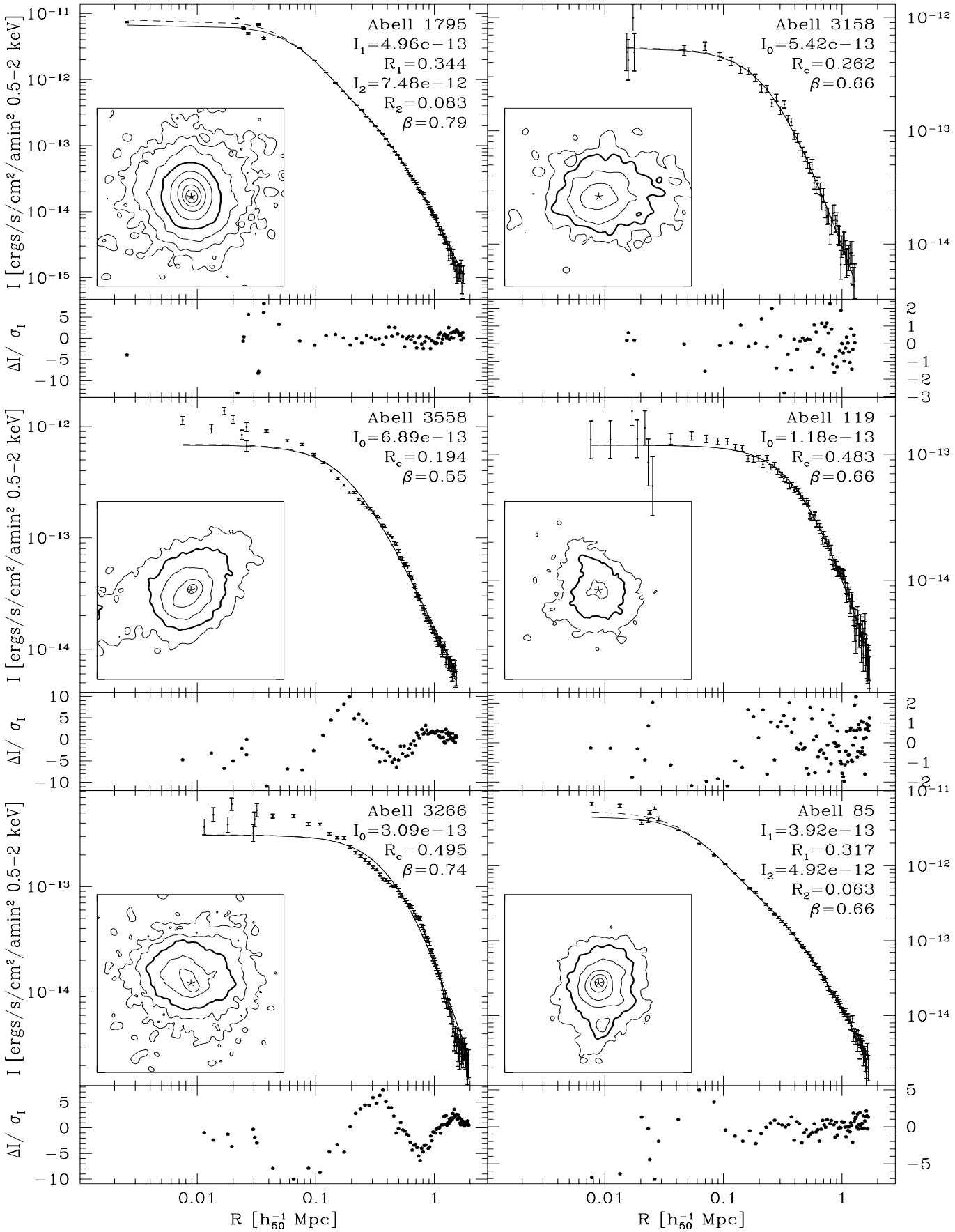

FIG. 6D.— A 1795, A 3158, A 3558, A 119, A 3266, A 85

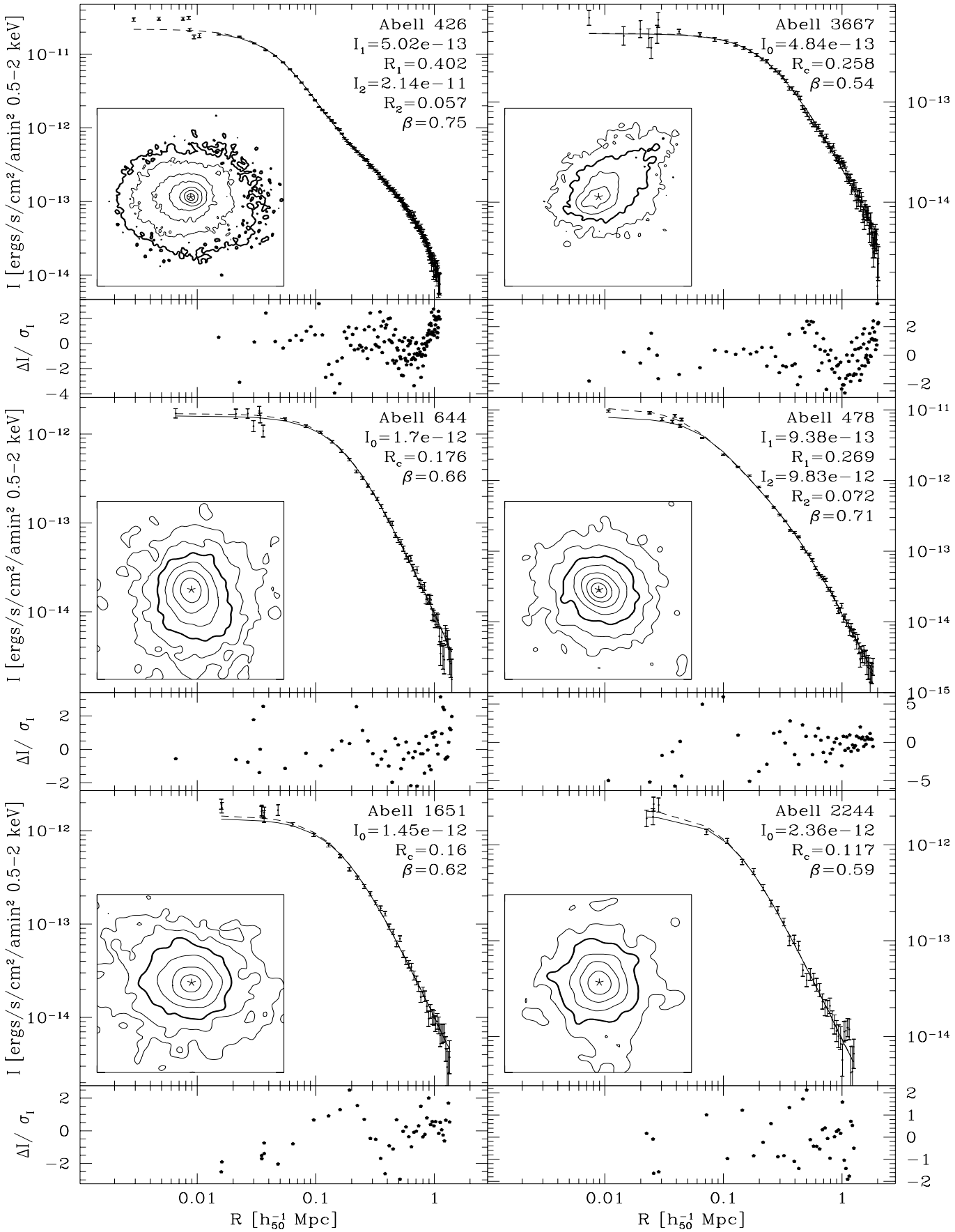

FIG. 6E.— A 426, A 3667, A 644, A 478, A 1651, A 2244

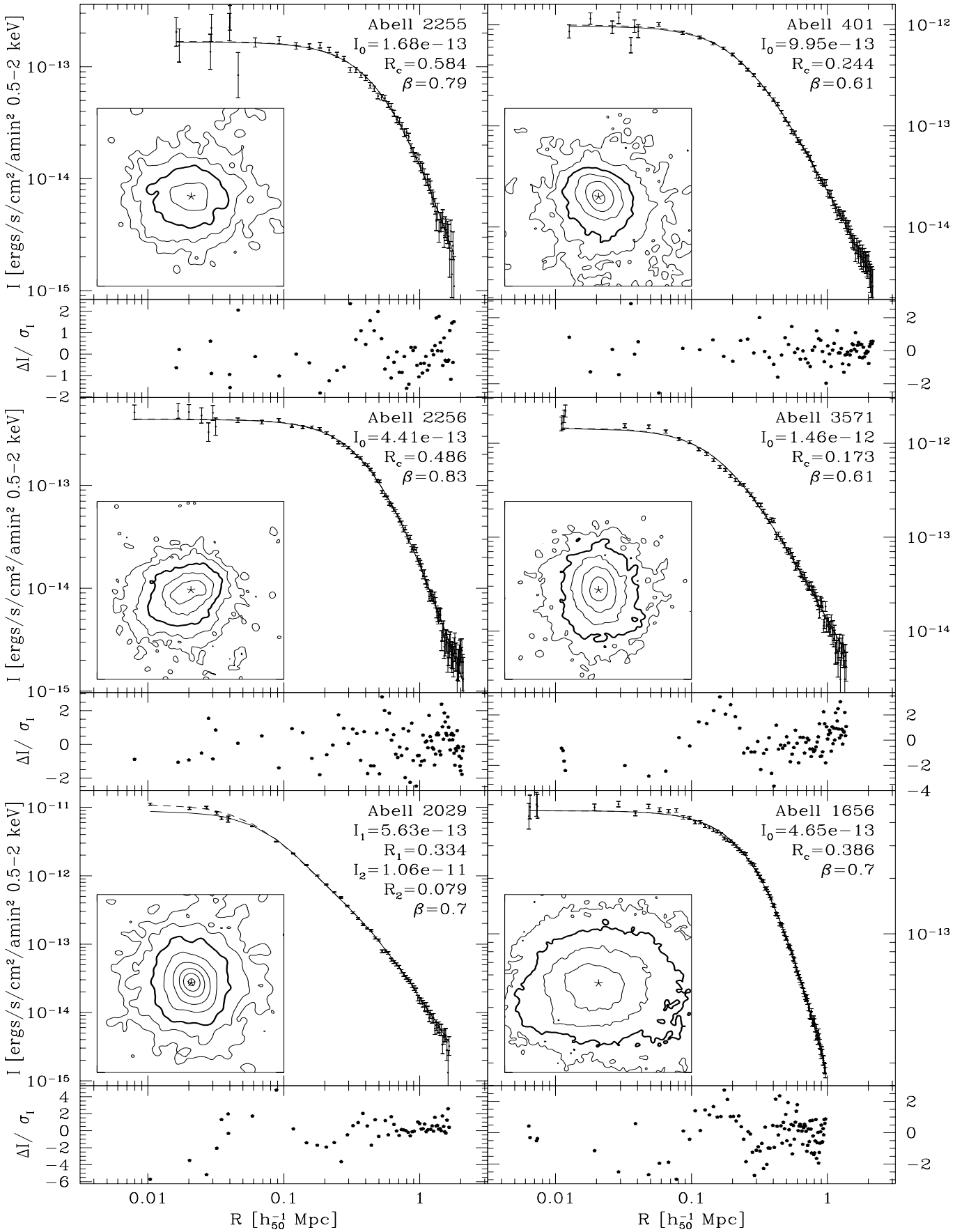

FIG. 6F.— A 2255, A 399, A 2256, A 3571, A 2029, A 1656

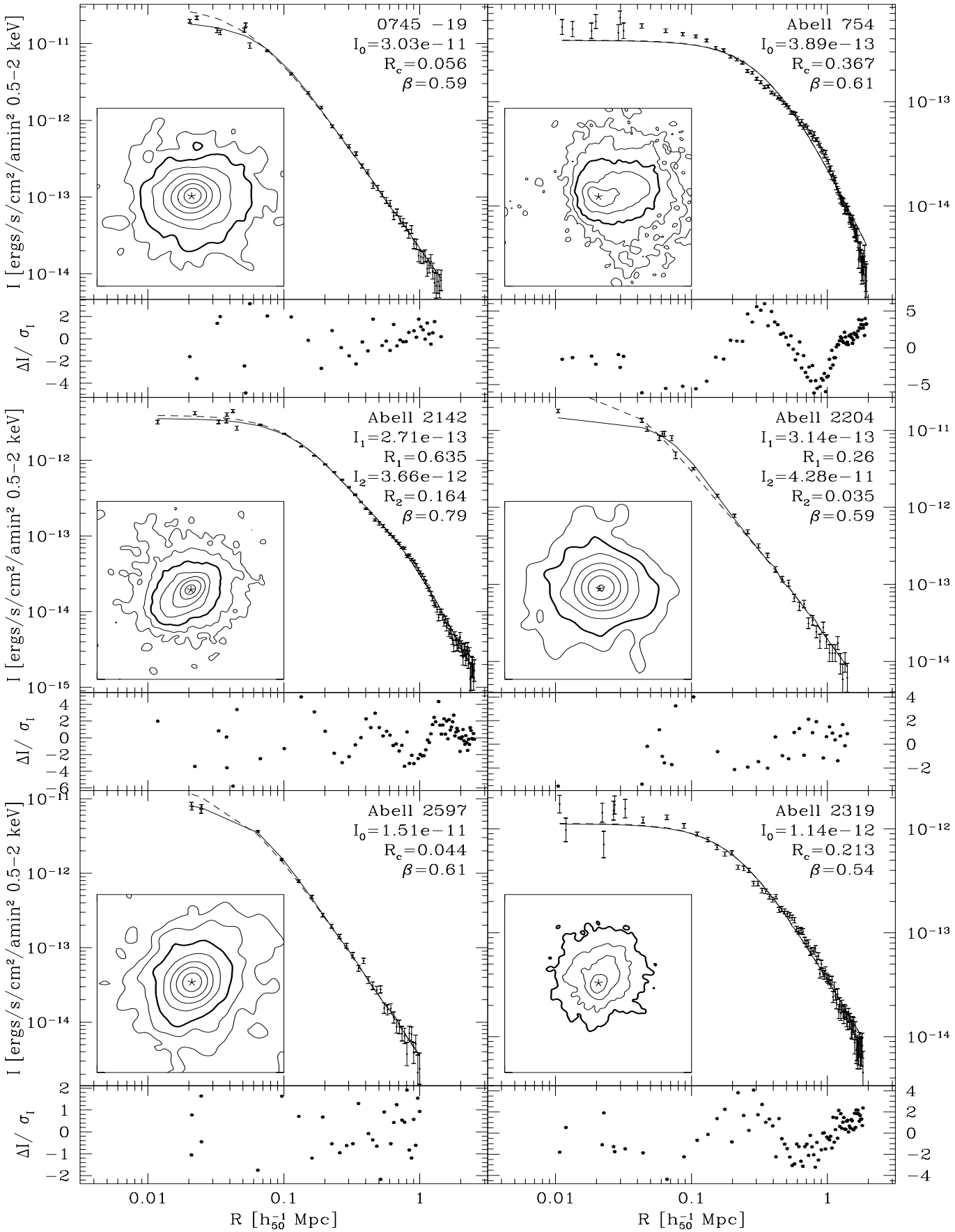

FIG. 6G.— 0745 -19, A 754, A 2142, A 2204, A 2597, A 2319

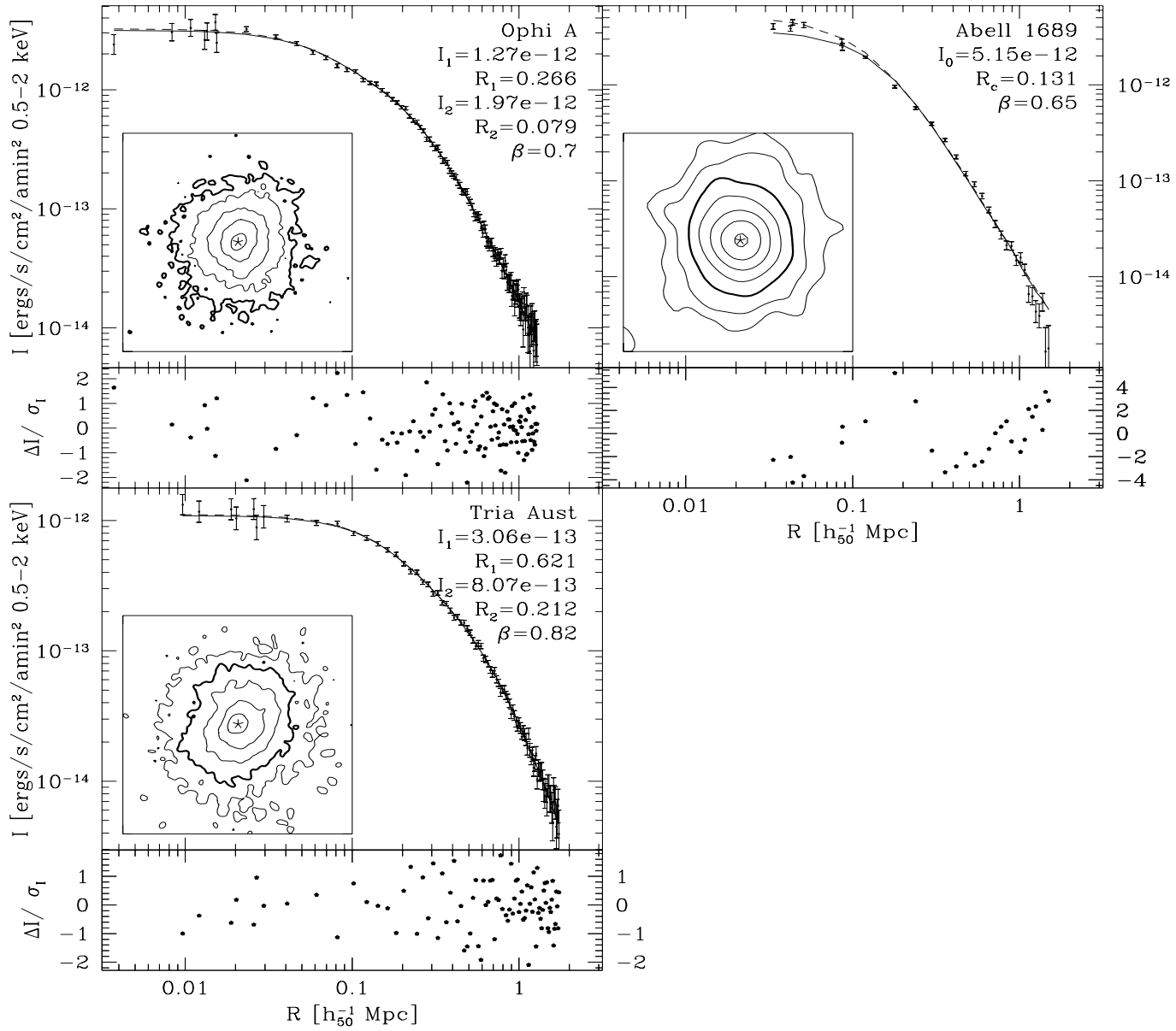

FIG. 6H.— Ophiucus, A 1689, Triangulum Australis; Cluster X–ray surface brightness profiles: For each cluster the radially averaged, unabsorbed surface brightness in units of ergs/s/cm^2/□′in the 0.5:2.0 keV band is plotted versus distance from the cluster emission center [in h_{50}^{-1} Mpc]. The surface brightness measurements (points with error bars), the underlying model (dashed line) and the PSF corrected model (solid line) are plotted. Residuals between the fit and the data (scaled by the data uncertainty) appear below each radial profile. A contour map of the portion of the cluster image used to calculate $I(R)$ appears in the lower left corner; the images are smoothed to facilitate contouring. The emission center is marked with a star; contours appear at factors of 2.5 in surface brightness, and the heavy contour corresponds to a fiducial surface brightness of 4.0×10^{-14} ergs/s/cm^2/□′in each cluster. The cluster name and best fit parameters appear in the upper right hand corner of each plot. Both sets of parameters are listed for those clusters fit with a two component β model.

A 1795.

$$r_{500} = 2.37 h_{50}^{-1}\ \mathrm{Mpc} \left(\frac{\langle T_X \rangle}{10\,\mathrm{KeV}}\right)^{1/2} \qquad (11)$$

$$M_{500} = 2.00 \times 10^{15} h_{50}^{-1} M_\odot \left(\frac{\langle T_X \rangle}{10\,\mathrm{KeV}}\right)^{3/2}$$

If our β model mass for A 1795 is in error, we will still be studying comparable regions of each cluster; those regions would have an enclosed overdensity different than 500 times the critical density.

Tables 3 and 4 contain the results. The columns in Table 3 correspond to cluster name, ICM central density ρ_0, central electron number density n_e, and the radial location $\langle r \rangle / r_{500}$ of a typical ICM particle located within r_{500}. Table 4 contains the ICM masses M_{ICM} and mass fractions f_{ICM}. The columns correspond to cluster name; M_{ICM} and f_{ICM} calculated within a limiting radius $r_{lim} = 1 h_{50}^{-1}$ Mpc; r_{500}, M_{ICM} and f_{ICM} calculated using the virial relation; and r_{500}, M_{ICM} and f_{ICM} calculated using the isothermal β model. All uncertainties correspond to 90% confidence limits (see §3.5).

4.2.1. *ICM Masses M_{ICM} and Mass Fractions f_{ICM}*

Fig. 7 contains a plot of M_{ICM} and f_{ICM}, calculated within a limiting radius r_{500}, versus emission weighted mean ICM temperature $\langle T_X \rangle$. The left panel contains results obtained using the isothermal β model to estimate binding masses and r_{500}, and the right panel contains results using the virial scaling relation (Eqn. 11). As noted above, measurements within r_{500} sample the same portion of each cluster's virial region, whereas measurements within a fixed metric radius are directly comparable to results from previous analyses and are more nearly independent of assumptions about the cluster potential.

Within r_{500} the best fit relation between M_{ICM} and $\langle T_X \rangle$ is

$$M_{ICM} = (1.49 \pm 0.09) \times 10^{14}\ M_\odot\ T_6^{1.98\pm0.18} \qquad (12)$$

where T_6 is $\langle T_X \rangle$ in units of 6 keV. The variance weighted RMS scatter in M_{ICM} around this relation is 17%; in calculating the variance weighted RMS, each cluster is weighted using its M_{ICM} measurement uncertainty. We find the best fit relation by minimizing χ^2, the sum of the squared, orthogonal deviations ν_i^2 of each point; ν_i is the minimum distance between point i and the fit scaled by one over σ_i, the point i uncertainty along that vector. We fit using only those 42 clusters with well determined temperature uncertainties, and we determine the 90% uncertainties on the fit parameters using 500 bootstrap fits.

The 17% scatter about this relation is another indicator of the regularity of galaxy clusters; the scatter is consistent with constraints derived from analysis of scatter in the Size-Temperature relation in an X-ray flux limited cluster sample (Mohr & Evrard 1997) and the luminosity-temperature relation in a cooling-flow free cluster sample

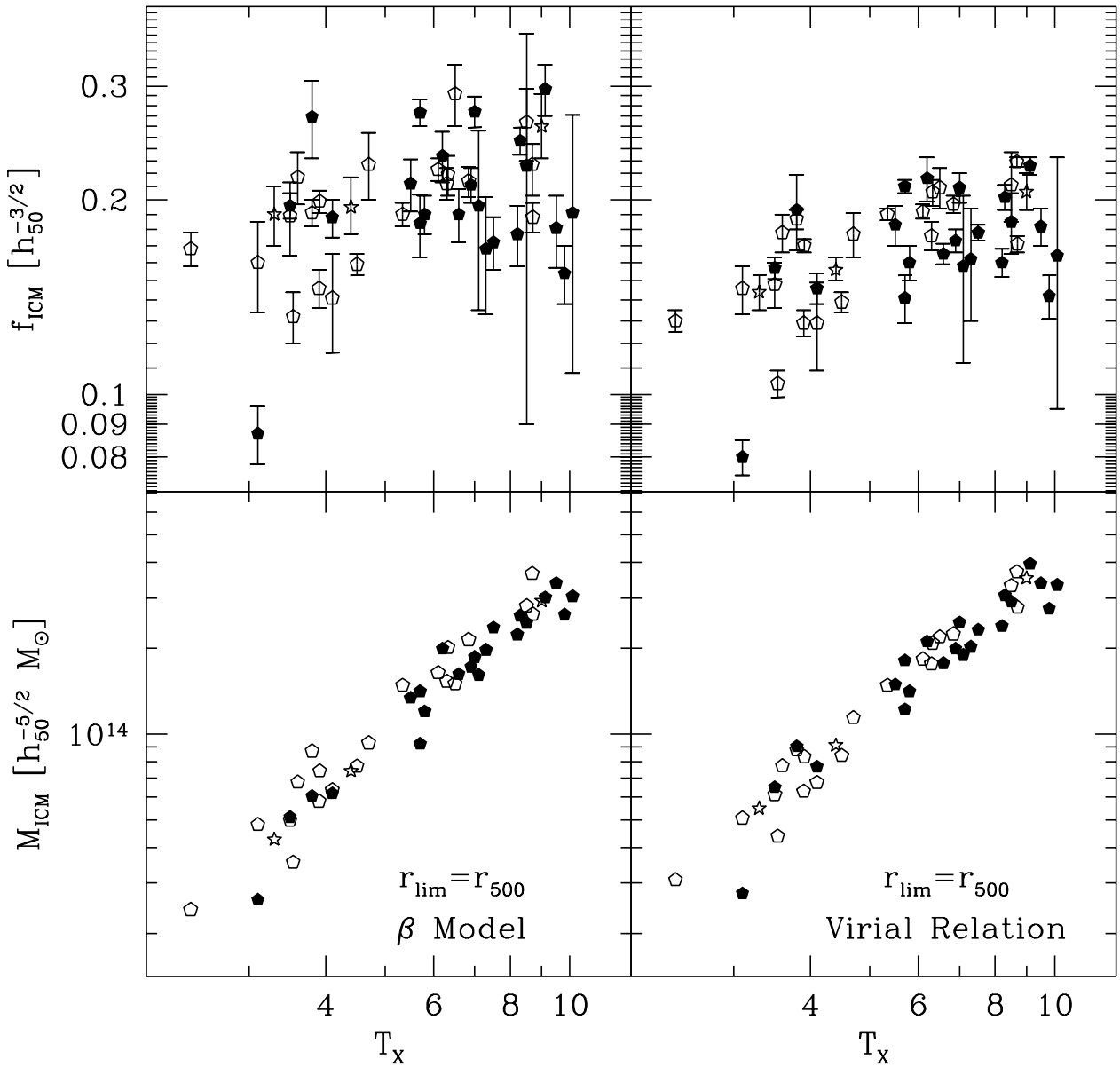

FIG. 7.— We plot ICM mass M_{ICM} (below) and mass fraction f_{ICM} (above) versus $\langle T_X \rangle$; these quantities are measured within the limiting radius $r_{lim} = r_{500}$, where r_{500} is calculated using the virial relation (left) and the isothermal β model (right; see §4.2 and Table 3). Different symbols represent clusters with central cooling times significantly below 10^{10} yrs (open), higher central cooling times (solid), and clusters with no upper limits on their $\langle T_X \rangle$ measurements (stars).

(Arnaud & Evrard 1998). The slope of this relation is steep; it is statistically inconsistent with a slope of $\frac{3}{2}$, the expectation if galaxy clusters are self similar objects. We also examine the M_{ICM}-$\langle T_X \rangle$ relation using measurements where r_{500} is determined using the virial theorem (see Eqn. 11). In comparison to the β model analysis, these data exhibit a somewhat smaller 14% scatter (see Fig 4.2.1), but a statistically consistent slope 1.94 ± 0.12.

The best fit f_{ICM}-$\langle T_X \rangle$ relation within r_{500} is

$$f_{ICM} = (0.207 \pm 0.011)\ T_6^{0.34\pm0.22} \quad (13)$$

where T_6 is $\langle T_X \rangle$ in units of 6 keV; the variance weighted scatter about the relation is 17%. These data provide evidence for a modest increase in f_{ICM} with $\langle T_X \rangle$. The slope is inconsistent with zero at the 99% confidence level. We probe for variations in f_{ICM} by dividing the sample at $\langle T_X \rangle = 5$ keV; the weighted mean of the 17 low $\langle T_X \rangle$ (28 high $\langle T_X \rangle$) clusters is 0.167±0.008 (0.212±0.006), corresponding to a statistically significant difference of 0.045±0.010 (uncertainties are 90% confidence intervals determined using RMS scatter of measurements about the mean). The mean f_{ICM} of the low $\langle T_X \rangle$ sample rises to 0.176±0.006 if A 1060 is excluded, bringing the difference in the mean of the two samples to 0.036±0.001. An analysis of f_{ICM} where r_{500} and M_{500} are calculated using a virial scaling relation suggests a slightly more rapid increase of f_{ICM} with $\langle T_X \rangle$. The best fit slope is 0.41±0.16, and f_{ICM} is larger in hot clusters than in cool ones by 0.052±0.009. We caution that the virial scaling relation assumes self similarity in the cluster population, but the measurements presented above demonstrate the ICM properties are inconsistent with self similarity. Therefore, it is a distinct possibility that the virial scaling relation masses M_{500} are systematically in error.

We have examined the same relations within a fixed radius of $1h_{50}^{-1}$ Mpc. The best fit relations between M_{ICM}, f_{ICM} and $\langle T_X \rangle$ are

$$M_{ICM} = (7.45 \pm 0.49) \times 10^{13}\ M_\odot\ T_6^{1.23\pm0.17} \quad (14)$$

$$f_{ICM} = (0.184 \pm 0.009)\ T_6^{0.17\pm0.17} \quad (15)$$

where T_6 is $\langle T_X \rangle$ in units of 6 keV. As expected, the M_{ICM}-$\langle T_X \rangle$ is shallower than the corresponding r_{500} relation presented above. The f_{ICM}-$\langle T_X \rangle$ relation is flatter and consistent with no increase of f_{ICM} with $\langle T_X \rangle$; this is primarily caused by a reduction in f_{ICM} in the higher $\langle T_X \rangle$ portion of the sample, behavior that implies an increasing f_{ICM} with radius.

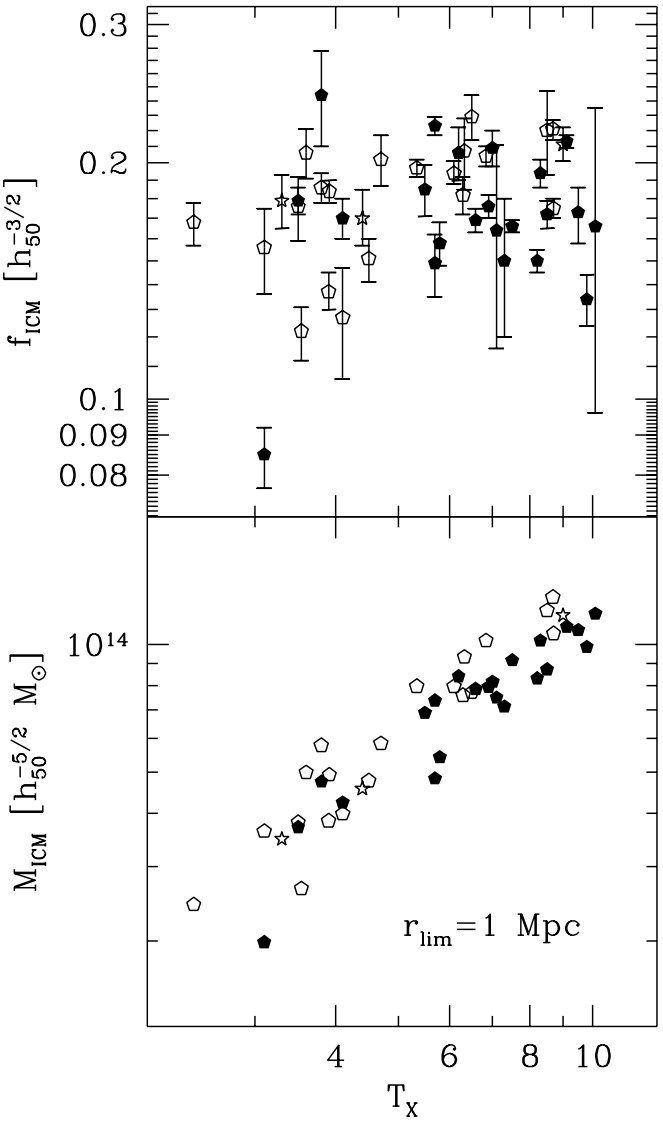

FIG. 8.— We plot ICM mass M_{ICM} (below) and mass fraction f_{ICM} (above) versus $\langle T_X \rangle$; these quantities are measured within the limiting radius $r_{lim} = 1h_{50}^{-1}$ Mpc. Clusters with different central cooling times are represented with different symbols as in Fig. 7.

In addition, the data suggest a different M_{ICM}-$\langle T_X \rangle$ zeropoint in short and long cooling time clusters; the zeropoint for the 20 short cooling time clusters is $8.19^{\pm0.81} \times 10^{13}$ $M_\odot$ and for the the 22 long cooling time clusters is $6.29^{\pm0.43} \times 10^{13}$ $M_\odot$. This corresponds to $\Delta M_{ICM} = 1.90^{\pm0.92} \times 10^{13}$ $M_\odot$, a 3.3σ or ∼25% offset. An offset of similar scale appears in measurements made within a $0.75h_{50}^{-1}$ Mpc aperture; $\Delta M_{ICM} = 1.32^{\pm0.65} \times 10^{13}$ $M_\odot$ which is a 3.2σ or ∼25% offset. At the larger radius r_{500} the offset is $\Delta M_{ICM} = 2.73^{\pm1.91} \times 10^{13}$ $M_\odot$ which is a 2.3σ or 18% offset.

This correlation between M_{ICM} and central cooling time could be because, at a particular mass scale or $\langle T_X \rangle$, clusters with higher gas content are more likely to experience central cooling instabilities; in that case we need to understand what mechanism drives the differences in gas content. Our numerical cluster simulations which include gravity and gas dynamics provide no evidence for

large M_{ICM} offsets like those observed. Alternatively, one might suggest that we are seeing the results of the ICM "flowing" into the cluster core; the scale of the mass offset requires an average flow rate of $\sim$2000 $M_\odot$/yr over the age of the universe, which makes this explanation unlikely. On the other hand, the higher M_{ICM} in clusters with shorter central cooling times may be an artifact; central cooling instabilities may enable the formation of a multiphase medium and significant ICM density and temperature variations rather than the smooth density distribution and isothermal ICM implicit in the β model analysis. These density variations enhance the X-ray emissivity, causing an increase in the X-ray luminosity and a bias in our estimates of the central density ρ_0 (see Eqn. 8). Quantitatively the offsets in M_{ICM} could be explained by a multiphase medium in short central cooling time clusters if that medium enhanced the X-ray luminosity by $\sim 50\%$ on average.

4.2.2. *ICM Radial Distribution*

We also probe for systematic differences in the radial distribution of the ICM in high and low $\langle T_X \rangle$ clusters. The presence of differences could be an indication that galactic winds have contributed significant energy to the ICM (White 1991, Metzler & Evrard 1994, Metzler & Evrard 1998). In past studies, discussion has focused on the value -3β, the asymptotic slope of the ICM; we take a new approach which incorporates the entire ICM distribution within the radius r_{500}. Specifically, we calculate the average radial location $\langle r \rangle / r_{500}$ of an ICM particle within the same physical region of each cluster, where

$$\langle r \rangle = \frac{\int_0^{r_{500}} d^3r \; r\rho(r)}{\int_0^{r_{500}} d^3r \; \rho(r)} \tag{16}$$

Differences in the ICM radial distribution with $\langle T_X \rangle$ will appear as trends in $\langle r \rangle / r_{500}$ versus $\langle T_X \rangle$.

Fig. 4.3 (lower panel) contains a plot of $\langle r \rangle / r_{500}$ versus $\langle T_X \rangle$ for our cluster sample. Symbols code central cooling times as in other figures. The distribution of $\langle r \rangle / r_{500}$ in this flux limited cluster sample provides no indication that the ICM is more extended in low mass clusters. These data stand in contrast to previous analyses of large *Einstein* IPC samples (e.g. Mohr et al. 1995) which indicated a tendency for low $\langle T_X \rangle$ clusters to have lower β's (more extended ICM distributions).

We have analyzed the entire sample with a single β model fit, and we recover a trend for lower $\langle T_X \rangle$ cluster to have a more extended ICM. Therefore, the root of the discrepancy between our results and previous results lies primarily in the treatment of the central emission excesses. Fig. 3.1 demonstrates the differences between single and double component β model fits to the X-ray data on A 1795, a cluster with a central emission excess. We plot the best fit single component model (dashed line), the double component model (solid line), the residuals around the fit (single: solid points, double: hollow points), and we list the best fit parameters and reduced χ^2. The behavior in A 1795 is generic to clusters with central emission excesses; the best fit single β model has a small core radius and correspondingly low β that grossly misrepresents the asymptotic behavior of the surface brightness profile. The two extra free parameters in the double β model fit allow the core and asymptotic behavior of the profile to be fit simultaneously; the gross trends in the residuals disappear and the goodness of fit parameter χ^2 falls by a factor of 5. As discussed in §3.1, adding the second component is similar in spirit to excluding the core region from the fit; however, results of fits to core excised clusters depend on the scale of the region excised, exposing the fit parameters to the subjective whims of the observer. We choose double β model fitting because it is more objective, and because our data demonstrate that the extra component allows the core and the asymptotic behavior of the profiles to both be fit simultaneously.

We also probe for trends in the ICM distribution with $\langle T_X \rangle$ using β_{eff}, a nonparametric measure of the slope of the surface brightness profile. Specifically,

$$\beta_{eff} = \frac{1}{3}\left[\frac{\log(I_i/I_o)}{\log(A_o/A_i)} + \frac{1}{2}\right]; \tag{17}$$

operationally, we choose an area A_o, find the isophote I_o which encloses that area, and then find the isophote I_i which encloses the area $A_i = 0.7A_o$. This approach yields the effective ICM falloff $-3\beta_{eff}$ over a particular annulus determined by A_o. Fig. 3.1 (upper panel) contains a plot of β_{eff} measured at r_{5000} versus $\langle T_X \rangle$ for the same sample; the data provide no indication that lower $\langle T_X \rangle$ clusters have a more extended ICM. Because β_{eff} changes with radius in a cluster (small in the core and steepening with radius) it is important that it be measured in the same physical region in each cluster (rather than at a particular isophote; see Mohr & Evrard 1997). The results displayed here are calculated at a radius $r = 0.75h_{50}^{-1}(\langle T_X \rangle / 10 \text{ keV})$ Mpc, corresponding to r_{5000} and $A_o = \pi r_{5000}^2$, a radius at which β_{eff} can be measured in each cluster image.

4.3. *Comparison to Previous Results*

We compare our M_{ICM} and f_{ICM} measurements to previously published results. Rather than present detailed notes on each cluster, we focus on two trends apparent from the comparisons. First, our measurements in the clusters fit with single β models are generally consistent with previously published results. Second, our measurements on clusters with central emission excesses tend to produce lower ICM masses M_{ICM} than previously published results. In individual cases of disagreement in β parameters, we invite the reader to examine the X-ray surface brightness profiles and contour plots (Fig. 6) as a way of gauging the plausibility of our fit (Allen et al. 1996, Bardelli et al. 1996, Breen et al. 1994, Briel et al. 1992, Briel & Henry 1996, Buote & Canizares 1996, Cirimele, Nesci & Trevese 1997, David, Jones & Forman 1995, Dell'Antonio, Geller & Fabricant 1995, Fabricant et al 1989, Henry et al. 1993, Henriksen & White 1996, Henriksen & Jones 1996, Makino 1994, Neumann & Boehringer 1995, Pislar et al. 1997, Sarazin & McNamara 1997, White & Fabian 1995).

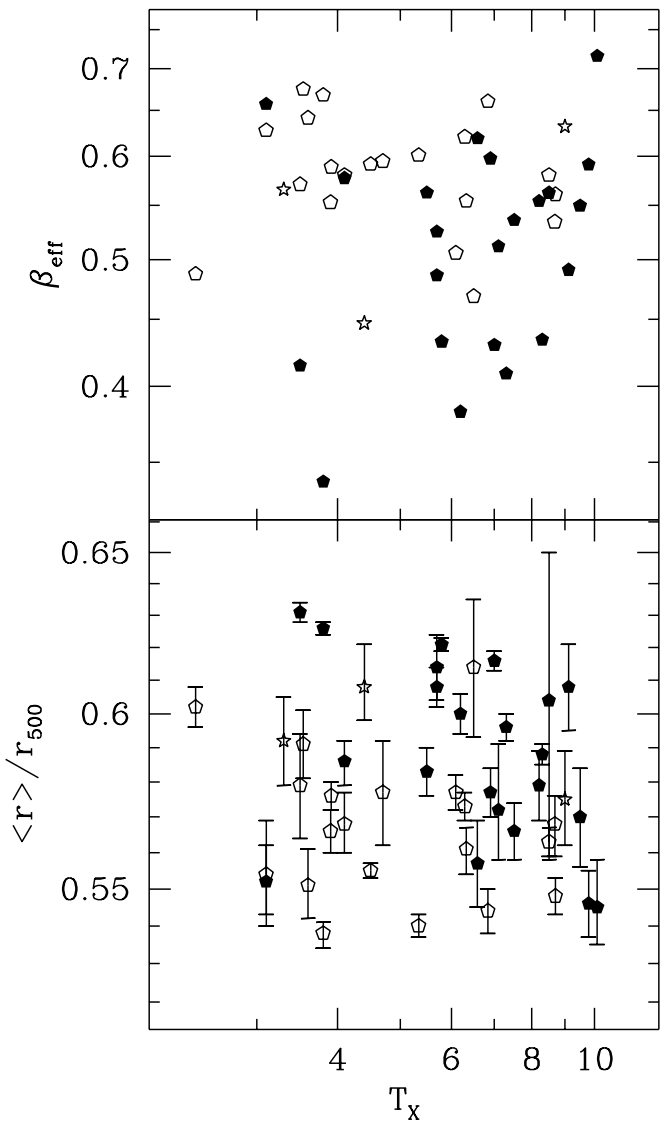

FIG. 9.— We plot the typical location of a gas particle within r_{500} (below) and β_{eff}, a nonparametric estimate of the radial falloff of the ICM calculated at $\sim r_{5000}$ (above). As before, symbols denote different central cooling times. Neither dataset provides evidence for a more extended ICM in low $\langle T_X \rangle$ clusters (see discussion in §4.2.2).

We have examined the issue of emission excesses in great detail; we analyze all clusters with central emission excesses using a single and double component β model. In the median, the double β model analysis provides an M_{ICM} which is 7% lower than the single β model analysis (maximum reduction is 20% in A 3526). This results because the emission excess biases the parameters R_c and β low in the single component fits. The works which reported higher ICM masses generally used a single-beta model approach and ignored the central emission excesses; in these cases we were able to demonstrate consistency by showing that we could match the author's result using a single-beta model ourselves. A few authors took the approach of excising the central region before fitting the cluster profile; these works generally show better agreement with our double-beta model results.

We also found four papers which do not follow the trends outlined above. Three of these (Durret et al 1994, Myers et al 1997, Fukumoto & Ikeuchi 1992) employ very different analyses, making it difficult to discern the source of the disagreement. The recent deprojection analysis of 207 cooling flows using IPC data (White, Jones & Forman 1997) presents ICM masses and mass fractions for many of our clusters and seems to employ a comparable method, but we found poor agreement between our results. There are 18 clusters which we both measure out to $1h^{-1}$ Mpc; out of this set, there are 9 clusters for which our uncertainty ranges in M_{ICM} do not overlap. Strangely, there is no evidence of a systematic difference in our results; when plotted against one another the scatter is just much larger than the error bars. Analysis of the ICM mass fractions f_{ICM} is even more discouraging, with only two clusters in agreement. Here, however, there is a systematic difference in that the fractions of WJF are almost all much lower than our own. The worst offenders are clusters for which WJF uses older X-ray temperature determinations (Cygnus A, A 2029, A 2142, A 2319, A 401 and A 496) or which have no measured velocity dispersions. The source of this discrepancy is still unclear, but seems to be due at least in part to the large uncertainties in the galaxy velocity dispersions σ_{gal}, which sets the depth of the potential well in their deprojection technique. As already mentioned in the introduction, calculating ICM masses and mass fractions does not require assumptions about the detailed shape of the cluster potential, and so we make none in our analysis.

To conclude, we reiterate that because the ICM distribution follows directly from the X-ray surface brightness profile, a model which provides a better fit to the data will yield a more accurate estimate of M_{ICM} (see §3. Extensive testing of the double beta model approach convinces us that the technique produces a significantly better description of the data, allowing simultaneous fitting of the core emission excess and the asymptotic behavior of the gas at the limiting radius of the data.

5. DISCUSSION

We analyze the X-ray and ICM properties of an essentially X-ray flux limited sample of 45 galaxy clusters. The fundamental observations are archival ROSAT PSPC images and published $\langle T_X \rangle$ measurements; we describe our techniques in §3 to facilitate reproducibility. Combining our data and an ensemble of numerical cluster simulations, we quantify the uncertainties in the measured quantities.

In addition to constraining the properties of the ICM in nearby clusters (see discussion below and §4), we include a set (see Fig. 6) of cluster X-ray surface brightness profiles in physical units along with contour plots of the cluster X-ray emission to help the reader evaluate the goodness of fit, the importance of substructure and the overall plausibility of the analysis in each cluster. While a few clusters in our sample are undergoing major mergers, making our analysis suspect, it should be remembered that our analysis of an ensemble of simulated clusters indicates that M_{ICM} can be estimated with a typical accuracy of $\sim$9% in coeval populations with similar morphologies to those observed (i.e. even with merging clusters included).

5.1. *ICM Regularity*

The observed scatter around the M_{ICM}-$\langle T_X \rangle$ and f_{ICM}-$\langle T_X \rangle$ relation is 17%; correcting the scatter for the 9%

observational contribution (derived from numerical simulations) reduces the scatter to 14%. This scatter is consistent with predictions made using the scatter around the cluster Size-Temperature relation (Mohr & Evrard 1997). The properties of this X-ray flux limited cluster sample provide further evidence that galaxy clusters are, on average, regular objects (see also Mohr & Evrard 1997, Arnaud & Evrard 1998). Interestingly, "exceptional" clusters do exist; A 1060 has an M_{ICM} and f_{ICM} which are low relative to clusters with similar $\langle T_X \rangle$ (see also Lowenstein & Mushotzky 1996).

5.2. *Self-similarity and Evidence for Galaxy Feedback*

Measurements of M_{ICM} at r_{500} provide evidence that the ICM content of galaxy clusters is not self-similar. Specifically, the slope of the M_{ICM}-$\langle T_X \rangle$ relation at r_{500} is 1.98±0.18 (90% confidence unless otherwise noted), different from the self-similarity expectation of $\frac{3}{2}$ at 4.3σ. We also probe for trends in f_{ICM} with $\langle T_X \rangle$. The best fit f_{ICM}-$\langle T_X \rangle$ relation has a slope of 0.34±0.22, and is inconsistent with no variation at 2.5σ. If the steep slope of the M_{ICM}-$\langle T_X \rangle$ relation were entirely caused by an increase of f_{ICM} with $\langle T_X \rangle$, the required f_{ICM}-$\langle T_X \rangle$ relation slope would be 0.48, well within the 90% confidence interval of our measurements; therefore, it is possible that the steep M_{ICM}-$\langle T_X \rangle$ slope is due solely to an increase of f_{ICM} with $\langle T_X \rangle$. We also examine trends in f_{ICM} by comparing clusters with $\langle T_X \rangle$ above and below 5 keV. We find that the 28 clusters with $\langle T_X \rangle > 5$ keV have f_{ICM}=0.212±0.006, 0.045±0.010 higher than the mean of the 17 low $\langle T_X \rangle$ clusters. Thus, these data indicate that f_{ICM} increases with $\langle T_X \rangle$, and that this increase may be responsible for the steepness of the M_{ICM}-$\langle T_X \rangle$ relation.

This departure from self similarity in the ICM properties of clusters could be a reflection of a lack of self similarity in the underlying dark matter distribution; the "universal" NFW density profile predicts significant departures from self similarity in the cluster population driven by earlier formation, on average, of low mass clusters when compared to high mass clusters (Navarro, Frenk, & White 1997). On the other hand, the ICM is sensitive to a wider range of physics than the dark matter, and this sensitivity might, in part, be responsible for the observed departures from self similarity. Energy injection into the intergalactic medium by supernovae driven galactic winds is one possible mechanism; a trend of increasing f_{ICM} with $\langle T_X \rangle$ is consistent with some models of galaxy feedback (Metzler & Evrard 1998, Tozzi, Cavaliere & Menci 1998). Another possibility is that the efficiency of galaxy formation varies with cluster mass (David et al. 1990, Arnaud et al 1992).

Interestingly, our extensive dataset provides no evidence that the ICM is more extended in low $\langle T_X \rangle$ clusters. Specifically, there are no apparent trends in the typical radial location $\langle r \rangle / r_{500}$ of an ICM particle within r_{500}, a non-parametric estimate of the radial fall-off of the ICM density β_{eff} at r_{5000}, or β measured fitting to the whole surface brightness profile. Previous analyses of large samples have relied primarily on single β model fitting, which we show (see Fig. 3.1 and §4.2) returns highly biased estimates of β and r_c in clusters with large, central emission excesses. This bias, combined with the greater prevalence of low $\langle T_X \rangle$ clusters with central emission excesses, leads to an artificial trend in β or $\langle r \rangle / r_{500}$ with $\langle T_X \rangle$. We recover this trend when we analyze our entire sample using solely single β model fits. Models of galaxy feedback generally produce a more extended ICM in low mass clusters (Metzler & Evrard 1998). While our data do not rule out a weak trend in ICM extent, they provide no suggestion that one exists above 2.4 keV.

5.3. *Constraints on* Ω_M

Under the fair sample hypothesis, baryon fraction measurements within cluster virial regions can be used to derive an unbiased estimate of the universal baryon fraction. By combining measurements of f_{ICM} in clusters (a lower limit on the cluster baryon fraction) with nucleosynthesis constraints on the baryon to photon ratio, we place an upper limit on the cosmological density parameter for clustered matter Ω_M (e.g. White et al. 1993).

Because more massive clusters are less affected by processes like galaxy feedback which might enhance ICM depletion within the cluster virial region, we use the mean f_{ICM} calculated in the $\langle T_X \rangle > 5$ keV subsample of 27 clusters: f_{ICM}=$0.212 h_{50}^{-3/2}$ (see §4.2.1). We apply two corrections to this mean f_{ICM}: (1) a correction for ICM depletion within r_{500} (driven by shocks during cluster formation), and (2) a correction for ICM clumping which causes an overestimate of f_{ICM}. We also use the numerical simulations to estimate ICM depletion within r_{500}; our ensemble of 48 simulations indicates that, on average, f_{ICM} within r_{500} is 12% lower than the cosmic value. As discussed in §3.5 and §4.2.1, ICM density variations or clumping enhance the X-ray luminosity and bias f_{ICM} estimates high. Analysis of our numerical simulations indicates that, on average, estimates of M_{ICM} and f_{ICM} are too high by 12%. There is no guarantee that the structure responsible for this overestimate in our simulations mimics the structure present in real clusters. Hot galactic winds, magnetic fields, and radiative cooling instabilities could well enhance density structure; in fact, larger variations in the ICM density distribution, and therefore larger systematic errors in M_{ICM}, are possible if the ICM has a strongly multi-phase structure (Gunn & Thomas 1996, Nagai, Sulkanen & Evrard in prep). Comparisons of cluster X-ray emission and the Sunyaev-Zel'dovich effect decrement in the cosmic microwave background should further constrain the density and temperature variations in the ICM.

Correcting the mean f_{ICM} for clumping and depletion (these corrections cancel), we get our best estimate of the cosmic ICM mass fraction: $f_{ICM} = (0.212 \pm 0.006) h_{50}^{-3/2}$, where the uncertainty represents the 90% confidence range from observational uncertainties (§3.5). Constraints on the clustered mass density parameter Ω_M are then

$$\Omega_M < \frac{\Omega_b}{\langle f_{ICM} \rangle} = (0.36 \pm 0.01) \Theta_{sys} h_{50}^{-1/2} \qquad (18)$$

where we have used $\Omega_b = (0.077 \pm 0.001) h_{50}^{-2}$ (Burles & Tytler 1998). The $\sim 3\%$ uncertainty reflects the observational uncertainty of the mean f_{ICM}; Θ_{sys} is a scale factor that represents systematic effects which we haven't addressed. Our analysis of an ensemble of 48 numerical cluster simulations suggests that after correcting for depletion and gas clumping, $\Theta_{sys} = 1$. Deviations of Θ_{sys} from 1

would reflect systematics which appear in real clusters but not in simulated clusters. Some possibilities are (1) very steep temperature profiles at r_{500} and (2) a very strong multiphase medium extending throughout the cluster. Recent comparisons of lensing mass estimates and isothermal β model binding mass estimates also suggest $\Theta_{sys} \sim 1$; the mean ratio of isothermal β model to lensing binding masses is 1.04±0.07 for the CNOC cluster sample (Lewis et al 1998). Additionally, cluster ICM masses M_{ICM} have an associated systematic uncertainty due to uncertainties in the absolute flux calibration of the ROSAT PSPC; we estimate that the PSPC absolute flux calibration is good to $\sim 15\%$, implying that ICM masses are uncertain by approximately 7.5%. Combining these estimates of systematic uncertainties yields $\Theta_{sys} = 1 \pm 0.10$. Future binding mass analyses of even larger cluster samples and observations from the well calibrated AXAF satellite (Elsner et al 1994) will further constrain Θ_{sys}.

We acknowledge helpful discussions with Michael Turner. This research makes use of the NASA/GSFC HEASARC Online Service, and benefits significantly from the efforts of the PROS software development team at the Smithsonian Astrophysical Observatory. This work is supported by NASA grants NAG5-3401 and NAGW-2367 and is supported through AXAF Fellowship grant PF8-1003, awarded through the AXAF Science Center. The AXAF Science Center is operated by the Smithsonian Astrophysical Observatory for NASA under contract NAS8-39073.

REFERENCES

Allen, S. W., Fabian, A. C., Johnstone, R. M., Nulsen, P. E. J. & Edge, A. C. 1992, MNRAS, 254, 51
Allen, S. W.; Fabian, A. C. & Kneib, J. P. 1996, MNRAS, 279, 615
Arnaud, M., Rothenflug, R., Boulade, O., Vigroux, L. & Vangioni–Flam, E. 1992, å, 254, 49.
Arnaud, M. & Evrard, A. E. 1998, MNRAS, submitted
Bardelli, S.; Zucca, E.; Malizia, A.; Zamorani, G.; Scaramella, R.; & Vettolani, G. 1996, A&A, 305, 435
Breen, J.; Raychaudhury, S.; Forman, W.; & Jones, C. 1994, ApJ, 424, 59
Briel, U. G.; Henry, J. P. & Böhringer H. 1992, A&A, 259, L31
Briel, U. G. & Henry J. P. 1996, ApJ, 472, 131
Buote, D.A. & Canizares, C.R. 1996, ApJ, 457, 565
Buote, D.A. & Xu, G. 1997, MNRAS, 284, 439
Burles, S. & Tytler, D. 1998, ApJ, 499, 699
Carlberg, R.G., Yee, H.K.C., Ellingson, E., Morris, S.L., Abraham, R., Gravel, P., Pritchet, C.J., Smecker-Hane, T., Hartwick, F.D.A., Hesser, J.E., Huychings, J.B., Oke, J.B. 1997, ApJ, 485, L13
Cavaliere, A. & Fusco-Femiano, R. 1978, A&A, 70, 677
Cavaliere, A., Menci, N. & Tozzi, P. 1998, astro-ph/9802185
Cirimele, G., Nesci, R. & Trevese, D. 1997, ApJ, 475, 11
David, L.P., Arnaud, K.A., Forman, W. & Jones, C. 1990, ApJ, 356, 32
David, L. P., Slyz, S. C., Forman, W., Vrtilek, S. D. & Arnaud, K. A. 1993, ApJ, 412, 479
David, L.P., Jones. C. & Forman, W. 1995, ApJ, 445, 578
Davis, M., Efstathiou, G., Frenk, C. S. & White, S. D. M. 1985, ApJ, 292, 371
Day, C. S. R., Fabian, A. C., Edge, A. C., Raychaudhury, S. 1991, MNRAS, 252, 394
Dell'Antonio, I.P., Geller, M.J. & Fabricant, D.G. 1995, AJ, 110, 502
Durret, F., Gerbal, D., Lachieze-Rey, M. & Sadat, R. 1994, A&A, 287, 733
Edge, A.C., Stewart, G.C., Fabian, A.C., & Arnaud, K.A. 1990, MNRAS, 245, 559
Elsner, R.F., Joy, M.K., Ramsey, B.D. & Weisskopf, M.C. 1994, Proc SPIE 2279, 332.
Evrard, A. E. 1988, MNRAS, 235, 911
Evrard, A. E. 1990, ApJ, 363, 349
Evrard, A.E., Metzler, C.A. & Navarro, J.F. 1996, ApJ, 469, 494
Evrard, A.E. 1997, MNRAS, 292, 289
Fabricant, D.G., Lecar, M. & Gorenstein, P. 1980, ApJ, 336, 77
Fabricant, D.G., Beers, T.C., Gorenstein, P., Huchra, J.P. & Kurtz, M.J. 1986, ApJ, 308, 530
Fabricant, D.G., Kent, S.M. & Kurtz, M.J. 1989, ApJ, 336, 77
Feldman, U. 1992, Physics Scripta 46, 202
Fukumoto, J. & Ikeuchi, S. 1992, PASJ, 44, L235
Gunn, K.F. & Thomas, P.A. 1996, MNRAS, 281, 1133
Henriksen, M. J. & Jones, C. 1996, ApJ, 465, 666
Henriksen, M. J. & Markevitch, M. L. 1996, ApJ, 466, L79
Henriksen, M.J. & White, R.E. 1996, ApJ, 465, 515
Henry, J. P.; Briel, U. G. & Nulsen, P. E. J. 1993, A & A, 271, 413
Hughes, J. P., Butcher, J. A., Stewart, G . C. & Tanaka, Y. 1993, ApJ, 404, 611
Johnstone, R. M., Fabian, A. C., Edge, A. C. & Thomas, P. A. 1992, MNRAS, 255, 431
Knopp, G.P., Henry, J.P., & Briel, U.G. 1996, ApJ, 472, 125
Lewis, A.D., Ellingson, E., Morris, S.L. & Carlberg, R.G. 1998, ApJ, submitted
Lowenstein, M. & Mushotzky, R.F. 1996, ApJ, 471, L83
Makino N. 1994, PASJ, 46, 139
Markevitch, M. 1996, ApJ, 465, L1
Markevitch, M. & Vikhlinin, A. 1997, ApJ, 474, 84
Markevitch, M., Forman, W.R., Sarazin, C.L. & Vikhlinin, A. 1998, ApJ, submitted
Matsuzawa, H., Matsuoka, M., Ikebe, Y., Mihara, T. & Yamashita, K. 1996, PASJ, 48, 565
Metzler, C. & Evrard, A.E. 1994 ApJ, 437, 564
Metzler, C. & Evrard, A.E. 1998 ApJ, submitted
Mohr, J.J., Fabricant, D.G. & Geller, M.J. 1993, ApJ, 413, 492
Mohr, J. J., Evrard, A. E., Fabricant, D. G. & Geller, M. J. 1995, ApJ, 447, 8
Mohr, J.J., Geller, M.J., Fabricant, D.G., Wegner, G., Thorstensen, J. & Richstone, D.O. 1996, ApJ, 470, 724
Mohr, J.J. & Evrard, A.E. 1997, ApJ, 491, 38
Mohr, J.J. & Wegner, G. 1997, AJ, 114, 25
Myers, S.T., Baker, J.E., Readhead, A.C.S., Leitch, E.M. & Herbig, T. 1997, ApJ, 485, 1
Navarro, J.F., Frenk, C.S. & White, S.D.M. 1997, ApJ, 490, 493
Neumann, D. M. & Böhringer H. 1995, A&A, 301, 865
Pildis, R.A., Bregman, J.N. & Evrard, A.E. 1995, ApJ, 443, 514
Pislar, V.; Durret, F.; Gerbal, D.; Lima Neto, G. D.; & Slezak E. 1997, A&A, 322, 53
Press, W.H., Flannery, B.P., Teukolsky, S.A. & Vetterling, W.T. 1988, *Numerical Recipes in C, Second Edition*, (Cambridge University Press: Cambridge)
Richstone, D.O., Loeb, A. & Turner, E. 1992, ApJ, 393, 477
Roettiger, K., Stone, J.M. & Mushotzky, R.F. 1998, ApJ, 493, 62
Saglia, R.P., Bertschinger, E., Baggley, G., Burstein, D., COlless, M., Davies, R.L., McMahan, R.K. & Wegner, G. 1993, MNRAS, 264, 961
Saglia, R.P. Bertschinger, E., Baggley, G., Burstein, D., Colless, M., Davies, R.L., McMahan, R.K. & Wegner, G. 1997, ApJS, 109, 79
Sarazin, C. L. & McNamara, B. R. 1997, ApJ, 480, 203
Schindler, A. 1996, A&A, 305, 756
Snowden, S.L., McCammon, D., Burrows, D.N. & Mendenhall, J.A. 1994, ApJ, 424, 714
Tamura et al. 1996, PASJ, 48, 671
Thomas, P.A., Colberg, J.M., Couchman, H.M.P., Efstathiou, G.P., Frenk, C.S., Jenkins, A.R., Nelson, A.H., Hutchings, R.M., Peacock, J.A., Pearce, F.R. & White, S.D.M. 1998, MNRAS, 296, 1061
Tozzi, P., Cavaliere, A., & Menci, N. 1998, astro-ph/9804026
Tyson, J.A., Kochanski, G.P. & Dell'Antonio, I.P. 1998, ApJ, 498, L107
White, R.E. 1991, ApJ, 367, 69
White, S.D.M., Navarro, J.F., Evrard, A.E. & Frenk, C.S. 1993, Nature, 366, 429
White, D.A. & Fabian, A.C. 1995, MNRAS, 273, 72
White, D.A., Jones, C. & Forman, W. 1997, MNRAS, 292, 419

TABLE 1
CLUSTER IMAGE INFORMATION AND $\langle T_X \rangle$

Cluster	Sequence #	t_{exp}	$\langle T_X \rangle$
A 85	wp800174	14778	$6.10^{+0.12}_{-0.12}$
	rp800250		
A 119	rp800251	14281	$5.80^{+0.36}_{-0.36}$
A 262	rp800254	8063	$2.41^{+0.03}_{-0.03}$
A 401	wp800182	13408	$8.30^{+0.31}_{-0.31}$
	wp800235		
A 426	rp800186	4435	$6.33^{+0.21}_{-0.18}$
A 478	wp800193	21345	$6.84^{+0.13}_{-0.13}$
A 496	rp800024	8117	$3.91^{+0.04}_{-0.04}$
A 644	wp800379n00	9535	$6.59^{+0.10}_{-0.10}$
A 754	rp800232n00	16125	$8.50^{+0.30}_{-0.30}$
	wp800160, wp800550		
A 780	rp800318n00	17255	$3.80^{+0.12}_{-0.12}$
A 1060	wp800200	14563	$3.10^{+0.15}_{-0.15}$
A 1367	rp800153n00	17705	$3.50^{+0.11}_{-0.11}$
A 1651	wp800353	7155	$6.30^{+0.30}_{-0.30}$
A 1656	rp800005	19401	$8.21^{+0.16}_{-0.16}$
A 1689	rp800248	13300	$10.10^{+5.40}_{-2.80}$
A 1795	rp800055	58809	$5.34^{+0.07}_{-0.07}$
	rp800105		
A 2029	rp800249	14767	$8.70^{+0.18}_{-0.18}$
	wp800161		
A 2052	rp800275	8331	$3.10^{+0.20}_{-0.20}$
	rp800275a01		
A 2063	wp800184	9613	$4.10^{+0.60}_{-0.60}$
A 2142	rp800233	23154	$8.68^{+0.12}_{-0.12}$
	wp150084, wp800096, wp800551n00		
A 2199	wp150083	47162	$4.50^{+0.20}_{-0.10}$
	wp800644n00		
A 2204	rp800281	5075	9.00
A 2244	rp800265n00	2863	$7.10^{+2.40}_{-1.50}$
A 2255	rp800512n00	12457	$7.30^{+1.70}_{-1.10}$
A 2256	wp100110	17105	$7.51^{+0.11}_{-0.11}$
A 2319	wp800073	3932	$9.12^{+0.09}_{-0.09}$
	wp800073a01		
A 2597	rp800112n00	6894	$3.60^{+0.12}_{-0.12}$
A 3112	rp800302n00	7240	$4.70^{+0.24}_{-0.24}$
A 3158	rp800310	2921	$5.50^{+0.30}_{-0.40}$
A 3266	rp800211n00	19810	$6.20^{+0.50}_{-0.40}$
	wp800552n00		
A 3391	wp800080	5529	$5.70^{+0.42}_{-0.42}$
A 3526	rp800607a01	9480	$3.54^{+0.08}_{-0.08}$
	wp800192		
A 3532	wp701155n00	7742	4.40
A 3558	rp800076n00	27788	$5.70^{+0.12}_{-0.12}$
A 3562	rp800237n00	18497	$3.80^{+0.50}_{-0.50}$
A 3571	rp800287	5465	$6.90^{+0.18}_{-0.18}$
A 3667	rp800234n00	11328	$7.00^{+0.36}_{-0.36}$
A 4038	wp800354n00	3207	3.30
A 4059	wp800175	5221	$4.10^{+0.18}_{-0.18}$
0745-19	rp800623n00	9050	$8.50^{+1.20}_{-0.80}$
AWM 7	wp800168	12603	$3.90^{+0.12}_{-0.12}$
Cygnus A	wp800622n00	8733	$6.50^{+0.36}_{-0.36}$
MKW 3S	rp800128	9228	$3.50^{+0.12}_{-0.12}$
Ophiucus	rp800279n00	3713	$9.80^{+0.61}_{-0.61}$
Tria-Aust	rp800280n00	6640	$9.50^{+0.42}$

TABLE 2
PARAMETERS FOR X–RAY SURFACE BRIGHTNESS PROFILES

Cluster	I_1[a] ergs/s/cm^2/□′	R_1 h_{50}^{-1}Mpc	I_2[a] ergs/s/cm^2/□′	R_2 h_{50}^{-1}Mpc	β	χ^2_ν	#	θ_m[′]
A 85	$3.92^{0.54}_{0.60}$e-13	$0.317^{0.054}_{0.047}$	$4.92^{0.79}_{0.63}$e-12	$0.063^{0.011}_{0.009}$	$0.662^{0.029}_{0.024}$	3.39	81	19.9
A 119	$1.18^{0.04}_{0.04}$e-13	$0.483^{0.028}_{0.028}$			$0.662^{0.023}_{0.022}$	1.21	97	23.7
A 262	$1.59^{0.48}_{0.46}$e-13	$0.135^{0.035}_{0.034}$	$2.87^{0.89}_{0.85}$e-12	$0.014^{0.004}_{0.004}$	$0.556^{0.027}_{0.025}$	1.75	97	23.7
A 401	$1.01^{0.08}_{0.05}$e-12	$0.237^{0.016}_{0.019}$			$0.606^{0.015}_{0.016}$	0.66	77	18.7
A 426	$5.02^{0.50}_{0.70}$e-13	$0.402^{0.035}_{0.034}$	$2.14^{0.19}_{0.19}$e-11	$0.057^{0.005}_{0.005}$	$0.748^{0.034}_{0.027}$	1.95	142	36.6
A 478	$9.38^{1.76}_{1.62}$e-13	$0.269^{0.045}_{0.045}$	$9.83^{1.65}_{1.62}$e-12	$0.072^{0.011}_{0.011}$	$0.713^{0.030}_{0.033}$	5.10	56	13.7
A 496	$3.78^{0.44}_{0.33}$e-13	$0.219^{0.017}_{0.019}$	$7.31^{0.72}_{0.85}$e-12	$0.033^{0.003}_{0.003}$	$0.650^{0.021}_{0.019}$	1.70	83	20.4
A 644	$1.70^{0.27}_{0.26}$e-12	$0.176^{0.035}_{0.034}$			$0.660^{0.048}_{0.048}$	1.52	53	12.7
A 754	$3.89^{0.85}_{0.85}$e-13	$0.367^{0.324}_{0.309}$			$0.614^{0.361}_{0.360}$	9.33	92	22.4
A 780	$7.03^{1.50}_{0.42}$e-13	$0.237^{0.013}_{0.024}$	$1.11^{0.05}_{0.18}$e-11	$0.047^{0.002}_{0.008}$	$0.766^{0.021}_{0.025}$	2.54	57	15.0
A 1060	$1.98^{0.15}_{0.16}$e-13	$0.164^{0.017}_{0.015}$	$3.70^{0.40}_{0.30}$e-13	$0.043^{0.005}_{0.004}$	$0.703^{0.044}_{0.036}$	1.13	114	27.9
A 1367	$8.41^{0.41}_{0.40}$e-14	$0.360^{0.046}_{0.043}$			$0.607^{0.044}_{0.042}$	1.64	132	32.4
A 1651	$1.45^{0.09}_{0.07}$e-12	$0.160^{0.009}_{0.009}$			$0.616^{0.012}_{0.013}$	1.62	43	10.5
A 1656	$4.65^{0.14}_{0.14}$e-13	$0.386^{0.026}_{0.026}$			$0.705^{0.046}_{0.046}$	1.38	99	24.9
A 1689	$5.15^{0.64}_{0.77}$e-12	$0.131^{0.022}_{0.014}$			$0.648^{0.035}_{0.024}$	6.24	25	6.2
A 1795	$4.96^{1.03}_{0.43}$e-13	$0.344^{0.024}_{0.035}$	$7.48^{0.49}_{0.84}$e-12	$0.083^{0.005}_{0.009}$	$0.790^{0.031}_{0.032}$	7.40	74	17.9
A 2029	$5.63^{1.37}_{0.48}$e-13	$0.334^{0.022}_{0.036}$	$1.06^{0.06}_{0.11}$e-11	$0.079^{0.004}_{0.009}$	$0.705^{0.030}_{0.028}$	2.96	56	14.0
A 2052	$3.35^{0.95}_{0.60}$e-13	$0.203^{0.045}_{0.042}$	$5.38^{1.19}_{1.29}$e-12	$0.039^{0.009}_{0.009}$	$0.712^{0.081}_{0.069}$	1.71	52	13.0
A 2063	$2.39^{0.70}_{0.33}$e-13	$0.255^{0.045}_{0.044}$	$8.94^{1.52}_{3.00}$e-13	$0.059^{0.012}_{0.020}$	$0.706^{0.051}_{0.047}$	0.83	72	17.2
A 2142	$2.71^{1.03}_{0.95}$e-13	$0.635^{0.213}_{0.198}$	$3.66^{1.27}_{1.19}$e-12	$0.164^{0.054}_{0.051}$	$0.787^{0.082}_{0.093}$	3.81	76	18.7
A 2199	$7.84^{0.74}_{0.58}$e-13	$0.162^{0.010}_{0.008}$	$4.34^{0.22}_{0.29}$e-12	$0.041^{0.002}_{0.002}$	$0.663^{0.012}_{0.008}$	4.54	116	28.4
A 2204	$3.14^{1.74}_{1.48}$e-13	$0.260^{0.106}_{0.098}$	$4.28^{2.28}_{2.00}$e-11	$0.035^{0.015}_{0.012}$	$0.585^{0.061}_{0.045}$	3.34	30	6.7
A 2244	$2.36^{0.75}_{0.70}$e-12	$0.117^{0.047}_{0.031}$			$0.594^{0.061}_{0.045}$	1.15	34	8.7
A 2255	$1.68^{0.08}_{0.08}$e-13	$0.584^{0.046}_{0.039}$			$0.792^{0.050}_{0.043}$	0.98	60	14.5
A 2256	$4.41^{0.10}_{0.10}$e-13	$0.486^{0.042}_{0.041}$			$0.828^{0.062}_{0.061}$	1.17	93	22.7
A 2319	$1.14^{0.21}_{0.21}$e-12	$0.213^{0.070}_{0.069}$			$0.536^{0.061}_{0.060}$	2.92	85	20.7
A 2597	$1.51^{0.26}_{0.27}$e-11	$0.044^{0.007}_{0.006}$			$0.612^{0.023}_{0.021}$	1.24	28	7.7
A 3112	$8.55^{4.89}_{4.67}$e-12	$0.049^{0.022}_{0.021}$			$0.562^{0.040}_{0.040}$	3.17	48	12.0
A 3158	$5.42^{0.54}_{0.51}$e-13	$0.262^{0.034}_{0.031}$			$0.657^{0.041}_{0.036}$	1.02	54	13.7
A 3266	$3.09^{0.28}_{0.27}$e-13	$0.495^{0.040}_{0.038}$			$0.744^{0.039}_{0.037}$	11.02	92	22.4
A 3391	$2.30^{0.31}_{0.26}$e-13	$0.216^{0.045}_{0.038}$			$0.541^{0.048}_{0.044}$	0.80	55	13.2
A 3526	$2.01^{0.72}_{0.67}$e-13	$0.138^{0.045}_{0.040}$	$8.52^{3.72}_{3.08}$e-12	$0.012^{0.005}_{0.004}$	$0.569^{0.035}_{0.036}$	2.90	138	33.6
A 3532	$2.04^{0.37}_{0.29}$e-13	$0.246^{0.073}_{0.057}$			$0.589^{0.086}_{0.062}$	0.95	50	12.0
A 3558	$6.89^{0.54}_{0.51}$e-13	$0.194^{0.028}_{0.027}$			$0.548^{0.029}_{0.029}$	12.40	82	19.9
A 3562	$5.62^{0.42}_{0.34}$e-13	$0.097^{0.006}_{0.007}$			$0.470^{0.007}_{0.007}$	1.38	79	19.2
A 3571	$1.46^{0.10}_{0.10}$e-12	$0.173^{0.016}_{0.015}$			$0.610^{0.024}_{0.024}$	1.98	84	21.2
A 3667	$4.84^{0.38}_{0.37}$e-13	$0.258^{0.026}_{0.025}$			$0.541^{0.016}_{0.016}$	1.73	98	23.9
A 4038	$1.84^{0.32}_{0.29}$e-12	$0.056^{0.012}_{0.011}$			$0.537^{0.033}_{0.033}$	1.35	63	15.5
A 4059	$1.61^{0.22}_{0.20}$e-12	$0.078^{0.011}_{0.011}$			$0.558^{0.019}_{0.020}$	1.51	51	12.5
0745-19	$3.03^{0.62}_{0.53}$e-11	$0.056^{0.006}_{0.006}$			$0.586^{0.008}_{0.009}$	2.89	36	9.5
AWM 7	$4.10^{0.39}_{0.42}$e-13	$0.195^{0.013}_{0.011}$	$1.36^{0.22}_{0.14}$e-12	$0.032^{0.005}_{0.002}$	$0.678^{0.030}_{0.029}$	2.58	130	31.9
Cygnus A	$3.97^{2.00}_{2.50}$e-11	$0.015^{0.049}_{0.015}$			$0.472^{0.057}_{0.057}$	2.42	63	16.2
MKW 3S	$2.90^{0.73}_{0.69}$e-12	$0.056^{0.015}_{0.015}$			$0.562^{0.038}_{0.038}$	2.60	44	10.7
Ophiuchus	$1.27^{0.29}_{0.15}$e-12	$0.266^{0.028}_{0.026}$	$1.97^{0.21}_{0.61}$e-12	$0.079^{0.008}_{0.025}$	$0.705^{0.036}_{0.032}$	0.81	112	27.4
Tria Aust	$3.06^{0.88}_{0.41}$e-13	$0.621^{0.076}_{0.088}$	$8.07^{0.83}_{1.44}$e-13	$0.212^{0.025}_{0.038}$	$0.816^{0.062}_{0.060}$	0.71	87	21.2

[a]Rest frame within 0.5-2.0 keV band

TABLE 3
ICM DENSITY AND DISTRIBUTION

Cluster	n_e $h_{50}^{1/2}$ g cm^{-3}	ρ_0 $h_{50}^{1/2}$ cm^{-3}	$\langle r \rangle / r_{500}$
A 85	$2.62^{0.17}_{0.22}$e-2	$5.10^{0.32}_{0.44}$e-26	$0.577^{0.005}_{0.005}$
A 119	$1.40^{0.04}_{0.04}$e-3	$2.72^{0.09}_{0.08}$e-27	$0.621^{0.002}_{0.002}$
A 262	$3.74^{0.28}_{0.19}$e-2	$7.29^{0.55}_{0.38}$e-26	$0.602^{0.006}_{0.006}$
A 401	$5.87^{0.43}_{0.27}$e-3	$1.14^{0.08}_{0.05}$e-26	$0.588^{0.003}_{0.003}$
A 426	$5.50^{0.27}_{0.45}$e-2	$1.07^{0.05}_{0.09}$e-25	$0.561^{0.007}_{0.006}$
A 478	$3.81^{0.33}_{0.15}$e-2	$7.42^{0.64}_{0.30}$e-26	$0.544^{0.006}_{0.006}$
A 496	$4.18^{0.33}_{0.14}$e-2	$8.15^{0.64}_{0.26}$e-26	$0.576^{0.004}_{0.004}$
A 644	$9.17^{0.40}_{0.39}$e-3	$1.79^{0.08}_{0.08}$e-26	$0.557^{0.012}_{0.012}$
A 754	$2.92^{0.08}_{0.08}$e-3	$5.68^{0.15}_{0.16}$e-27	$0.604^{0.046}_{0.046}$
A 780	$4.77^{0.68}_{0.20}$e-2	$9.30^{1.32}_{0.40}$e-26	$0.538^{0.004}_{0.003}$
A 1060	$8.50^{0.51}_{0.54}$e-3	$1.66^{0.10}_{0.11}$e-26	$0.552^{0.009}_{0.010}$
A 1367	$1.25^{0.04}_{0.03}$e-3	$2.44^{0.08}_{0.07}$e-27	$0.631^{0.003}_{0.003}$
A 1651	$8.80^{0.40}_{0.39}$e-3	$1.71^{0.08}_{0.08}$e-26	$0.573^{0.004}_{0.004}$
A 1656	$3.12^{0.04}_{0.05}$e-3	$6.07^{0.07}_{0.09}$e-27	$0.579^{0.010}_{0.010}$
A 1689	$2.17^{0.23}_{0.24}$e-2	$4.22^{0.45}_{0.47}$e-26	$0.545^{0.010}_{0.013}$
A 1795	$2.99^{0.46}_{0.15}$e-2	$5.83^{0.89}_{0.29}$e-26	$0.540^{0.003}_{0.003}$
A 2029	$3.67^{0.59}_{0.18}$e-2	$7.14^{1.14}_{0.36}$e-26	$0.548^{0.005}_{0.005}$
A 2052	$3.42^{0.67}_{0.28}$e-2	$6.67^{1.31}_{0.55}$e-26	$0.554^{0.014}_{0.015}$
A 2063	$1.16^{0.24}_{0.09}$e-2	$2.25^{0.46}_{0.17}$e-26	$0.568^{0.008}_{0.009}$
A 2142	$1.58^{0.17}_{0.24}$e-2	$3.08^{0.34}_{0.46}$e-26	$0.568^{0.009}_{0.008}$
A 2199	$2.92^{0.18}_{0.15}$e-2	$5.68^{0.36}_{0.30}$e-26	$0.555^{0.002}_{0.002}$
A 2204	$1.17^{0.17}_{0.13}$e-1	$2.27^{0.34}_{0.26}$e-25	$0.575^{0.013}_{0.014}$
A 2244	$1.32^{0.19}_{0.29}$e-2	$2.58^{0.37}_{0.57}$e-26	$0.572^{0.014}_{0.019}$
A 2255	$1.74^{0.07}_{0.06}$e-3	$3.38^{0.14}_{0.13}$e-27	$0.596^{0.004}_{0.004}$
A 2256	$3.02^{0.05}_{0.05}$e-3	$5.89^{0.10}_{0.09}$e-27	$0.566^{0.008}_{0.008}$
A 2319	$6.21^{0.23}_{0.36}$e-3	$1.21^{0.05}_{0.07}$e-26	$0.608^{0.013}_{0.013}$
A 2597	$5.19^{0.73}_{0.75}$e-2	$1.01^{0.14}_{0.15}$e-25	$0.551^{0.009}_{0.010}$
A 3112	$3.61^{0.46}_{0.30}$e-2	$7.04^{0.89}_{0.58}$e-26	$0.577^{0.015}_{0.015}$
A 3158	$4.15^{0.28}_{0.26}$e-3	$8.08^{0.54}_{0.51}$e-27	$0.583^{0.007}_{0.007}$
A 3266	$2.38^{0.07}_{0.07}$e-3	$4.63^{0.14}_{0.14}$e-27	$0.600^{0.006}_{0.006}$
A 3391	$2.73^{0.30}_{0.28}$e-3	$5.31^{0.59}_{0.54}$e-27	$0.614^{0.010}_{0.010}$
A 3526	$6.81^{0.78}_{0.43}$e-2	$1.33^{0.15}_{0.08}$e-25	$0.591^{0.010}_{0.010}$
A 3532	$2.49^{0.34}_{0.27}$e-3	$4.86^{0.66}_{0.53}$e-27	$0.608^{0.010}_{0.013}$
A 3558	$4.95^{0.18}_{0.15}$e-3	$9.65^{0.34}_{0.29}$e-27	$0.608^{0.006}_{0.006}$
A 3562	$5.88^{0.39}_{0.26}$e-3	$1.15^{0.08}_{0.05}$e-26	$0.626^{0.002}_{0.002}$
A 3571	$7.92^{0.23}_{0.29}$e-3	$1.54^{0.05}_{0.06}$e-26	$0.577^{0.007}_{0.007}$
A 3667	$3.64^{0.13}_{0.13}$e-3	$7.09^{0.25}_{0.25}$e-27	$0.616^{0.003}_{0.003}$
A 4038	$1.43^{0.12}_{0.08}$e-2	$2.78^{0.23}_{0.16}$e-26	$0.592^{0.013}_{0.013}$
A 4059	$1.19^{0.09}_{0.06}$e-2	$2.31^{0.18}_{0.13}$e-26	$0.586^{0.007}_{0.006}$
0745 -19	$6.84^{0.45}_{0.58}$e-2	$1.33^{0.09}_{0.11}$e-25	$0.563^{0.004}_{0.004}$
AWM 7	$1.82^{0.06}_{0.11}$e-2	$3.54^{0.12}_{0.21}$e-26	$0.566^{0.006}_{0.006}$
Cygnus A	$1.29^{0.36}_{0.18}$e-1	$2.52^{0.71}_{0.34}$e-25	$0.614^{0.021}_{0.021}$
MKW 3S	$1.87^{0.14}_{0.10}$e-2	$3.65^{0.27}_{0.20}$e-26	$0.579^{0.015}_{0.015}$
Ophiuchus	$1.58^{0.25}_{0.14}$e-2	$3.08^{0.48}_{0.27}$e-26	$0.546^{0.009}_{0.009}$
Tria Aust	$6.57^{1.22}_{0.62}$e-3	$1.28^{0.24}_{0.12}$e-26	$0.570^{0.014}_{0.014}$

TABLE 4
ICM MASSES AND MASS FRACTIONS

	$r_{lim} = 1h_{50}^{-1}$ Mpc		Virial Relation at r_{500}			β Model at r_{500}		
Cluster	M_{ICM} $h_{50}^{-5/2}$ $M_\odot$	f_{ICM} $h_{50}^{-3/2}$	r_{lim} h_{50}^{-1} Mpc	M_{ICM} $h_{50}^{-5/2}$ $M_\odot$	f_{ICM} $h_{50}^{-3/2}$	r_{lim} h_{50}^{-1} Mpc	M_{ICM} $h_{50}^{-5/2}$ $M_\odot$	f_{ICM} $h_{50}^{-3/2}$
A 85	$7.95^{0.12}_{0.12}$e+13	$0.194^{0.006}_{0.007}$	1.873	$1.83^{0.03}_{0.03}$e+14	$0.192^{0.005}_{0.005}$	1.719	$1.64^{0.04}_{0.03}$e+14	$0.223^{0.009}_{0.009}$
A 119	$5.42^{0.06}_{0.06}$e+13	$0.158^{0.010}_{0.010}$	1.826	$1.41^{0.05}_{0.05}$e+14	$0.160^{0.010}_{0.010}$	1.635	$1.20^{0.05}_{0.05}$e+14	$0.190^{0.013}_{0.013}$
A 262	$2.44^{0.06}_{0.06}$e+13	$0.168^{0.011}_{0.010}$	1.177	$3.08^{0.11}_{0.11}$e+13	$0.130^{0.005}_{0.005}$	0.998	$2.42^{0.05}_{0.06}$e+13	$0.168^{0.010}_{0.010}$
A 401	$1.02^{0.02}_{0.02}$e+14	$0.194^{0.008}_{0.008}$	2.185	$3.06^{0.08}_{0.08}$e+14	$0.202^{0.009}_{0.009}$	1.934	$2.60^{0.07}_{0.07}$e+14	$0.247^{0.012}_{0.012}$
A 426	$9.33^{0.07}_{0.07}$e+13	$0.207^{0.022}_{0.021}$	1.908	$2.08^{0.08}_{0.07}$e+14	$0.206^{0.010}_{0.009}$	1.849	$2.01^{0.04}_{0.04}$e+14	$0.219^{0.016}_{0.015}$
A 478	$1.02^{0.02}_{0.02}$e+14	$0.204^{0.006}_{0.006}$	1.983	$2.24^{0.05}_{0.05}$e+14	$0.197^{0.006}_{0.006}$	1.901	$2.14^{0.04}_{0.05}$e+14	$0.214^{0.012}_{0.011}$
A 496	$4.93^{0.06}_{0.06}$e+13	$0.184^{0.006}_{0.006}$	1.500	$8.32^{0.17}_{0.17}$e+13	$0.170^{0.004}_{0.004}$	1.369	$7.42^{0.12}_{0.11}$e+13	$0.199^{0.008}_{0.008}$
A 644	$7.85^{0.20}_{0.20}$e+13	$0.169^{0.006}_{0.006}$	1.947	$1.77^{0.06}_{0.06}$e+14	$0.165^{0.006}_{0.006}$	1.805	$1.62^{0.03}_{0.03}$e+14	$0.190^{0.018}_{0.018}$
A 754	$8.72^{0.89}_{0.89}$e+13	$0.172^{0.007}_{0.007}$	2.211	$2.91^{0.31}_{0.31}$e+14	$0.185^{0.020}_{0.020}$	1.953	$2.45^{0.44}_{0.44}$e+14	$0.226^{0.136}_{0.136}$
A 780	$5.78^{0.05}_{0.05}$e+13	$0.186^{0.008}_{0.008}$	1.478	$8.79^{0.18}_{0.18}$e+13	$0.187^{0.007}_{0.006}$	1.464	$8.70^{0.17}_{0.18}$e+13	$0.191^{0.009}_{0.009}$
A 1060	$1.99^{0.05}_{0.05}$e+13	$0.085^{0.008}_{0.007}$	1.335	$2.76^{0.15}_{0.15}$e+13	$0.080^{0.005}_{0.005}$	1.273	$2.62^{0.08}_{0.08}$e+13	$0.087^{0.009}_{0.009}$
A 1367	$3.71^{0.06}_{0.06}$e+13	$0.179^{0.007}_{0.007}$	1.419	$6.50^{0.15}_{0.15}$e+13	$0.157^{0.006}_{0.006}$	1.216	$5.11^{0.28}_{0.28}$e+13	$0.196^{0.009}_{0.009}$
A 1651	$7.58^{0.10}_{0.09}$e+13	$0.182^{0.010}_{0.010}$	1.903	$1.76^{0.05}_{0.05}$e+14	$0.176^{0.009}_{0.009}$	1.706	$1.53^{0.04}_{0.04}$e+14	$0.212^{0.012}_{0.012}$
A 1656	$8.31^{0.08}_{0.08}$e+13	$0.150^{0.005}_{0.005}$	2.173	$2.39^{0.11}_{0.11}$e+14	$0.160^{0.008}_{0.008}$	2.056	$2.23^{0.03}_{0.03}$e+14	$0.177^{0.019}_{0.019}$
A 1689	$1.18^{0.02}_{0.03}$e+14	$0.166^{0.070}_{0.069}$	2.410	$3.33^{0.72}_{0.71}$e+14	$0.164^{0.069}_{0.069}$	2.221	$3.04^{0.64}_{0.64}$e+14	$0.191^{0.083}_{0.080}$
A 1795	$7.96^{0.06}_{0.06}$e+13	$0.197^{0.005}_{0.005}$	1.752	$1.48^{0.02}_{0.02}$e+14	$0.190^{0.004}_{0.004}$	1.752	$1.48^{0.03}_{0.03}$e+14	$0.190^{0.008}_{0.008}$
A 2029	$1.06^{0.01}_{0.01}$e+14	$0.175^{0.005}_{0.005}$	2.237	$2.78^{0.06}_{0.06}$e+14	$0.171^{0.005}_{0.005}$	2.128	$2.63^{0.05}_{0.05}$e+14	$0.188^{0.010}_{0.010}$
A 2052	$3.63^{0.09}_{0.10}$e+13	$0.156^{0.020}_{0.019}$	1.335	$5.07^{0.31}_{0.31}$e+13	$0.146^{0.013}_{0.012}$	1.276	$4.81^{0.20}_{0.19}$e+13	$0.160^{0.026}_{0.025}$
A 2063	$3.99^{0.05}_{0.05}$e+13	$0.127^{0.021}_{0.020}$	1.536	$6.76^{0.55}_{0.55}$e+13	$0.129^{0.020}_{0.020}$	1.458	$6.36^{0.50}_{0.50}$e+13	$0.141^{0.025}_{0.024}$
A 2142	$1.29^{0.06}_{0.06}$e+14	$0.221^{0.007}_{0.006}$	2.234	$3.70^{0.04}_{0.04}$e+14	$0.229^{0.004}_{0.004}$	2.206	$3.65^{0.22}_{0.24}$e+14	$0.227^{0.024}_{0.017}$
A 2199	$4.77^{0.03}_{0.03}$e+13	$0.151^{0.010}_{0.009}$	1.609	$8.40^{0.16}_{0.16}$e+13	$0.139^{0.005}_{0.005}$	1.493	$7.71^{0.14}_{0.14}$e+13	$0.159^{0.006}_{0.006}$
A 2204	$1.17^{0.04}_{0.04}$e+14	$0.211^{0.010}_{0.011}$	2.275	$3.52^{0.22}_{0.23}$e+14	$0.206^{0.013}_{0.014}$	1.979	$2.93^{0.12}_{0.14}$e+14	$0.260^{0.028}_{0.032}$
A 2244	$7.49^{0.26}_{0.25}$e+13	$0.164^{0.048}_{0.047}$	2.021	$1.89^{0.29}_{0.29}$e+14	$0.158^{0.046}_{0.045}$	1.782	$1.61^{0.23}_{0.23}$e+14	$0.196^{0.061}_{0.060}$
A 2255	$7.13^{0.09}_{0.09}$e+13	$0.150^{0.030}_{0.030}$	2.049	$2.02^{0.20}_{0.20}$e+14	$0.162^{0.032}_{0.032}$	2.008	$1.97^{0.20}_{0.20}$e+14	$0.168^{0.035}_{0.034}$
A 2256	$9.17^{0.16}_{0.16}$e+13	$0.166^{0.003}_{0.003}$	2.078	$2.32^{0.06}_{0.06}$e+14	$0.178^{0.005}_{0.005}$	2.113	$2.36^{0.03}_{0.03}$e+14	$0.172^{0.016}_{0.016}$
A 2319	$1.10^{0.05}_{0.05}$e+14	$0.213^{0.004}_{0.004}$	2.290	$3.95^{0.12}_{0.12}$e+14	$0.226^{0.007}_{0.007}$	1.911	$3.01^{0.20}_{0.20}$e+14	$0.297^{0.027}_{0.027}$
A 2597	$4.99^{0.17}_{0.17}$e+13	$0.206^{0.015}_{0.015}$	1.439	$7.73^{0.48}_{0.48}$e+13	$0.178^{0.012}_{0.012}$	1.290	$6.78^{0.27}_{0.27}$e+13	$0.217^{0.020}_{0.020}$
A 3112	$5.84^{0.16}_{0.16}$e+13	$0.202^{0.015}_{0.015}$	1.644	$1.14^{0.07}_{0.07}$e+14	$0.177^{0.014}_{0.014}$	1.412	$9.30^{0.33}_{0.33}$e+13	$0.227^{0.027}_{0.027}$
A 3158	$6.89^{0.12}_{0.12}$e+13	$0.185^{0.014}_{0.014}$	1.778	$1.49^{0.06}_{0.06}$e+14	$0.183^{0.013}_{0.013}$	1.632	$1.34^{0.06}_{0.06}$e+14	$0.212^{0.020}_{0.019}$
A 3266	$8.40^{0.15}_{0.15}$e+13	$0.206^{0.016}_{0.016}$	1.888	$2.11^{0.09}_{0.09}$e+14	$0.216^{0.017}_{0.017}$	1.801	$1.99^{0.09}_{0.09}$e+14	$0.234^{0.021}_{0.021}$
A 3391	$4.83^{0.12}_{0.12}$e+13	$0.149^{0.014}_{0.013}$	1.810	$1.22^{0.07}_{0.07}$e+14	$0.141^{0.012}_{0.012}$	1.511	$9.24^{0.59}_{0.56}$e+13	$0.184^{0.021}_{0.020}$
A 3526	$2.66^{0.06}_{0.06}$e+13	$0.122^{0.010}_{0.009}$	1.427	$4.38^{0.21}_{0.20}$e+13	$0.104^{0.005}_{0.005}$	1.227	$3.55^{0.07}_{0.06}$e+13	$0.132^{0.012}_{0.012}$
A 3532	$4.57^{0.13}_{0.13}$e+13	$0.170^{0.013}_{0.015}$	1.591	$9.13^{0.36}_{0.39}$e+13	$0.156^{0.006}_{0.007}$	1.378	$7.42^{0.59}_{0.53}$e+13	$0.195^{0.018}_{0.022}$
A 3558	$7.37^{0.16}_{0.16}$e+13	$0.223^{0.006}_{0.006}$	1.810	$1.81^{0.03}_{0.03}$e+14	$0.210^{0.005}_{0.005}$	1.524	$1.41^{0.05}_{0.05}$e+14	$0.273^{0.013}_{0.013}$
A 3562	$4.75^{0.11}_{0.11}$e+13	$0.244^{0.034}_{0.034}$	1.478	$9.04^{0.65}_{0.65}$e+13	$0.193^{0.026}_{0.026}$	1.157	$6.05^{0.44}_{0.44}$e+13	$0.269^{0.037}_{0.037}$
A 3571	$7.93^{0.09}_{0.09}$e+13	$0.176^{0.006}_{0.006}$	1.992	$1.99^{0.06}_{0.06}$e+14	$0.173^{0.007}_{0.007}$	1.776	$1.72^{0.03}_{0.03}$e+14	$0.211^{0.013}_{0.013}$
A 3667	$8.16^{0.10}_{0.10}$e+13	$0.209^{0.011}_{0.011}$	2.006	$2.46^{0.07}_{0.07}$e+14	$0.209^{0.011}_{0.011}$	1.673	$1.86^{0.07}_{0.07}$e+14	$0.274^{0.015}_{0.015}$
A 4038	$3.48^{0.08}_{0.08}$e+13	$0.179^{0.014}_{0.014}$	1.378	$5.48^{0.36}_{0.36}$e+13	$0.144^{0.009}_{0.009}$	1.156	$4.27^{0.07}_{0.07}$e+13	$0.190^{0.020}_{0.020}$
A 4059	$4.24^{0.07}_{0.07}$e+13	$0.170^{0.010}_{0.010}$	1.536	$7.68^{0.28}_{0.28}$e+13	$0.146^{0.008}_{0.008}$	1.313	$6.19^{0.17}_{0.17}$e+13	$0.188^{0.013}_{0.012}$
0745-19	$1.20^{0.03}_{0.03}$e+14	$0.220^{0.027}_{0.027}$	2.211	$3.31^{0.23}_{0.22}$e+14	$0.211^{0.026}_{0.026}$	1.940	$2.81^{0.18}_{0.18}$e+14	$0.264^{0.034}_{0.033}$
AWM 7	$3.84^{0.04}_{0.04}$e+13	$0.137^{0.007}_{0.008}$	1.498	$6.29^{0.23}_{0.23}$e+13	$0.129^{0.006}_{0.006}$	1.400	$5.81^{0.13}_{0.13}$e+13	$0.146^{0.010}_{0.010}$
Cygnus A	$7.70^{0.76}_{0.75}$e+13	$0.229^{0.015}_{0.015}$	1.933	$2.19^{0.11}_{0.11}$e+14	$0.209^{0.015}_{0.015}$	1.523	$1.50^{0.14}_{0.14}$e+14	$0.292^{0.032}_{0.032}$
MKW 3S	$3.81^{0.10}_{0.10}$e+13	$0.176^{0.017}_{0.016}$	1.419	$6.13^{0.47}_{0.47}$e+13	$0.148^{0.012}_{0.012}$	1.219	$4.98^{0.15}_{0.15}$e+13	$0.189^{0.025}_{0.024}$
Ophiuchus	$9.85^{0.12}_{0.12}$e+13	$0.134^{0.010}_{0.010}$	2.374	$2.75^{0.15}_{0.15}$e+14	$0.142^{0.011}_{0.011}$	2.270	$2.62^{0.10}_{0.10}$e+14	$0.154^{0.016}_{0.016}$
Tria Aust	$1.08^{0.02}_{0.02}$e+14	$0.173^{0.015}_{0.013}$	2.337	$3.37^{0.18}_{0.18}$e+14	$0.182^{0.012}_{0.012}$	2.340	$3.38^{0.11}_{0.12}$e+14	$0.181^{0.024}_{0.022}$